Inorganic Chemistry

pubs.acs.org/IC

Article

The Key Role of Monovalent Indium and Anionic Vacancies in Oxyfluorides Inducing Fluoride Ion Mobility and Luminescence

Alizée Deslandes, Fouad Alassani, Stanislav Péchev, Véronique Jubera, Mathieu Duttine, Jacinthe Gamon, Antoine Villesuzanne, Leïlou Loiseau-Foucher, Etienne Durand, Alexandre Fargues, and Alain Demourgues*

Cite This: *Inorg. Chem.* 2026, 65, 3270−3285

Read Online

ACCESS | Metrics & More | Article Recommendations | Supporting Information

ABSTRACT: Novel $Ba_{2-x}Sr_xInO_3F$ Ruddlesden−Popper phases were synthesized by solid-state routes at high temperatures under Ar and dry air. The structural features were determined through XRD analysis of well-crystallized powders and isolated single crystals. Two In sites were identified with various occupancies, dependent on the Sr content and on the atmosphere applied during annealing. This indium site distribution leads to the consideration of an anionic disorder on the apical site in the vicinity of In. A maximum in the O2−In−O2 bond angles is identified for the $Ba_{1.2}Sr_{0.8}InO_3F$ composition and corresponds to a stronger hybridization between the In (s,p) and O(p) orbitals in the equatorial plane, which should be the signature of monovalent indium. ^{19}F MAS NMR investigation recorded at various temperatures shows the F^- hopping phenomenon in the mixed (Ba/Sr) environment, which is most present in the $Ba_{1.2}Sr_{0.8}InO_3F$ oxyfluoride and linked to the presence of anionic vacancies. Considering the electroneutrality of the composition, monovalent indium should be stabilized in octahedron with a vacant vertex. Excitation (UV range) and emission (visible range) broad bands are clearly detected, but neither excitation nor emission wavelength varies with the Sr content. However, the photoluminescence intensity is strongly correlated with the composition and reaches a maximum for the $Ba_{1.2}Sr_{0.8}InO_3F$ compound. Density functional theory calculations allow for the identification of defect states related to anionic vacancies in the band gap, with hybridization mainly between In(s) and O(p) orbitals in the basal plane, thus explaining the self-trapped exciton (STE) mechanism.

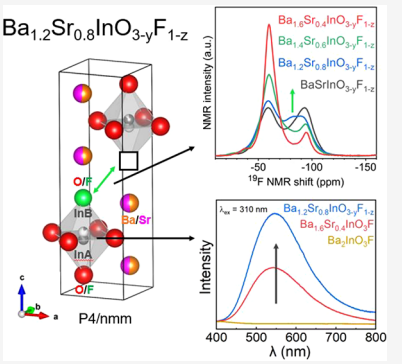

1. INTRODUCTION

Lead-based halides with a 3D perovskite network are widely investigated as semiconductors for optoelectronic applications, such as light emitting diodes (LED) with high photoluminescence efficiency, photodetectors, and solar cells with high quantum yield.

Because of the toxicity of lead,[1] the exploration of lead-free compounds and lone pair elements such as Bi^{3+} $(6s^2)$, $Sb^{3+}(5s^2)$, Sn^{2+} $(5s^2)$, or In^+ $(5s^2)$ is necessary for an array of applications.[2−6]

In lead-free halides such as elpasolite, Bi^{3+} $(6s^2)$ can substitute Sn^{4+} in Cs_2SnCl_6.[5] Low-dimensional structures, such as elpasolites, facilitate the B (Sn^{4+}, Bi^{3+}) octahedral site distortion[7] in double perovskites with A_2BX_6-type formula. This allows for the formation of localized electrons and holes, which is reflected in an efficient self-trapped exciton (STE) luminescence.[8] Increasing the dimensionality of the network contributes to the formation of an energy barrier formation between free exciton (FE) and STE defects.[9−11] The emission wavelength is strongly influenced by the local environments in the Cs_2MCl_6 series (with M a metal) with a green (512 nm) emission seen in the Cs_3InCl_6 host matrix and an orange one (596 nm) in Cs_2InCl_5, H_2O[12] upon Sb^{3+} $(5s^2)$ doping.[13,14] In a series of lead-free halides ranging from chloride ($Cs_2AgInCl_6$) with double-perovskite structure,[15] bromide (Cs_4SnBr_6) in the form of a 0D material with isolated $[SnBr_6]^{4-}$ octahedra,[16] and finally iodide ($Cs_3Cu_2I_5$), a 0D network with $[Cu_2I_5]^{3-}$ clusters,[17] a broadband STE emission is observed in the red, green, and blue regions, respectively.

In the case of complex oxide 3D perovskites with oxygen nonstoichiometry, such as Ba_2YAlO_5 or $Ba_6Y_2Al_4O_{15}$,[18] $Sn^{2+}(5s^2)$ centers are located in three different Ba^{2+} sites. This leads to the observation of a UV emission band centered at 360 nm and a blue emission at 460 nm for Ba_2YAlO_5 and $Ba_6Y_2Al_4O_{15}$, respectively. The A-band exhibits a clear doublet structure in absorption, which is still synonymous with the Jahn−Teller distortion.

In the case of mixed anions, working on oxyhalogenides is often challenging because, in a first scenario, each anion can be

Received: September 12, 2025
Revised: January 12, 2026
Accepted: January 14, 2026
Published: January 29, 2026

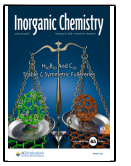

located around specific cationic sites with various emitters, while another option is for all of the anions to surround the same cationic center. In this latter case, the noncentrosymmetric character of the luminescent emitter site can be heightened, leading to a strong emission band. Such an anionic distribution is often related to the electronegativity, polarizability, and ionic size of each anion, which contributes to the modification of the energy bands far or near the Fermi level through competitive ionic and covalent bonds.[19]

A mixed situation can be evidenced in antiperovskite networks where two anions can be in the vicinity of a larger polarizable cation, whereas only one, often oxygen, is stabilized around the polarizing cations in tetrahedral symmetry. As such, annealing under a reducing atmosphere of the $Sr_{3-x}A_xMO_4F$ antiperovskite (A = Ca, Ba; M = Al, Ga, In)[20] stabilizes anionic vacancies, most likely on the F site. This leads to the formation of intrinsic defects at the origin of self-activated photoluminescence with a broadband orange emission.

For the $Ba_{n+1}In_n(O,F)_{3n+1}$ (n = 1−2) compounds, which are In-based oxyfluorides with 2D layer perovskite network, also named Ruddlesden−Popper (RP) phases, oxide and fluoride anions can be located on different crystallographic sites, leading to the Ba_2InO_3F ($P4/nmm$)[21] and $Ba_3In_2O_5F_2$ ($I4/mmm$)[22] specific formulas. These compounds are sensitive to moisture and exhibit transport properties through a significant amount of proton defects.[23] For all compositions, on the basis of bond valence calculations, O^{2-} ions are placed on the summits of a square pyramidal site. In this polyhedron, the In−O bond length is around 2.10 Å while the In−F bond length is much larger at 2.60−2.70 Å.[22,24] Extending the series to Sr_2FeO_3X (X = F, Cl, Br) oxyhalides, which adopt the ordered $P4/nmm$ structure,[25] F^- and O^{2-} anions are still ordering among the apical positions of the In^{3+} octahedra. In contrast, Sr_2MnO_3F,[26] Sr_2CoO_3F,[27] and Sr_2NiO_3F[28] can only be synthesized under high pressure and present the $I4/mmm$ structure with O and F disorder among the apical sites.[29] While Sr_2FeO_3F shows a well-behaved O/F ordered structure,[30] a recent investigation[31] showed that $Fe^{3+} \rightarrow Fe^{4+}$ oxidation leads to long-range anionic disorder on the apical site, accompanied by various O/F atomic ratios. Anionic disorder is also detected in stoichiometric Sr_2FeO_3F synthesized under high pressure.[32]

Anionic order/disorder in such mixed-anion compounds with 2D layer perovskite structures is a key feature, as it can induce anionic mobility, transport properties (electron and ionic conductivity), optoelectronic processes, and optical activity for d^{10} cations such as In^{3+}. The stabilization of In^+ ($4d^{10}$ $5s^2$), with its lone pair, is well established in the InX monohalogenides with $Cmcm$ space group (X= Cl, Br, I),[33−35] where the $[InX_5]^{4-}$ anionic group adopts a square pyramidal C_{4v} geometry. The increase of dimensionality (2D Ruddlesden−Popper, n = 1 → 3D perovskite, n = ∞) from n = 1 (Ba_2InO_3F) to n = 2 ($Ba_3In_2O_5F_2$) RP oxyfluorides leads to the formation of In^{3+}-based square pyramids and to a larger reduction in In−F apical bond length, from 2.7 to 2.6 Å, respectively.[22,24] This geometry is favorable for the $5s^2$ (In^+) lone pair stabilization.

For a p-element like indium, another way to induce anionic (O,F) disorder into the apical site, thus affecting the In site and allowing the stabilization of a lone pair (In^+), could be a simple partial substitution of Ba^{2+} in Ba_2InO_3F for a smaller alkaline earth such as Sr^{2+}. In this case, chemical pressure could also contribute to a reduction in the volume of the unit cell.

This work deals with the solid-state synthesis of the $Ba_{2-x}Sr_xInO_{3-y}F_{1-z}$ solid solution, performed at high temperature under Ar and followed eventually by heating under dry air. Single-crystal and powder X-ray diffraction analysis allow for the accurate determination of unit cell parameters, atomic positions, and bond lengths. ^{19}F MAS NMR investigation was undertaken in this series in order to probe the F local environments and their evolution versus the Sr content but also to investigate the possibility of fluorine mobility. Finally, taking into account the probable presence of In^{3+}/In^+ crystallographic sites in this RP network, as well as the occurrence of anionic vacancies inducing electronic defects stabilized within the band gap, photoluminescence experiments were carried out. The correlation between composition (the main variables are Sr composition and anionic vacancies), structural features, F mobility, and luminescence properties will be discussed. Finally, with the help of density functional theory (DFT) calculations performed on modeled defect structures (anionic vacancies), our aim is to emphasize the association between In^+ and V_{O2}-/V_{F}- vacancies in the RP phase and the photoluminescence properties.

2. EXPERIMENTAL SECTION

2.1. Solid-State Synthesis

This synthesis process is inspired by the works of Tarasova and Animitsa[36] on the Ba_2InO_3F and $Ba_3In_2O_5F_2$ Ruddlesden−Popper phases but was optimized by our team for the $Ba_{2-x}Sr_xInO_3F$ series.

Oxide and fluoride precursors BaF_2 (Prolabo, 99.99%), $BaCO_3$ (Merck ProAnalysis 99.99%), $SrCO_3$ (Optipur 99.99%), and In_2O_3 (Sigma-Aldrich, 99.99%) were weighed in stoichiometric amounts to yield 1.5 g of the final product. BaF_2 was chosen instead of SrF_2 because of its higher reactivity, linked to its lower melting point. Barium fluoride presents several hazards, primarily related to its toxicity if swallowed or inhaled, and its potential to cause irritation to the eyes and skin. They were then mixed together in an agate mortar for 5 min before being heat-treated in a tubular furnace on an alumina boat under argon flow. The decarbonation treatment was performed for 12 h at 800 °C, with heating and cooling ramps of 200 °C/h. Upon cooling, the powders were once again ground together for 5 min under air, then put into pellet form using a mechanical press (3 tons, 5 min). The pellets were then introduced in a tubular furnace and heat-treated under argon at 1050 °C for 24 h, with a 2 °C/min heating and cooling rate. The pellets were then directly moved to a glovebox because of their hygroscopic character. A routine powder XRD measurement was performed at this stage but showed incomplete reaction. Another identical heat treatment was thus performed on the samples, ground and pelletized for a second time. Part of the resulting powder was isolated to select small single crystals (∼20−50 μm) for XRD analysis. The approximate yield of the syntheses is between 94% and 100% depending on the impurity ($SrIn_2O_4$ and $(Ba,Sr)F_2$) rates around 3% each.

When studying the influence of the synthesis atmosphere on the resulting compound, part of the powder was reintroduced at this stage into the tubular furnace and fired at 1050 °C under dry air flow for 24 h.

2.2. Powder X-ray Diffraction

Laboratory powder X-ray diffraction (XRD) was used to check the purity of all compounds using a PANalytical X'Pert PRO diffractometer with a Cu Kα1,2 radiation (λ = 1.542 Å), at 45 kV and 40 mA. Measurements were conducted at room temperature between 2θ of 8 and 80° on rotating 0.4 mm diameter capillaries, with a wall thickness of 0.1 mm. The powders were introduced and sealed in the capillaries inside an argon-filled glovebox. To complete these acquisitions, synchrotron powder XRD acquisition was performed on the same capillaries for the x = 0.8 and the x = 0.6 samples. The measurements were conducted on the CRISTAL beamline at

https://doi.org/10.1021/acs.inorgchem.5c04288
Inorg. Chem. 2026, 65, 3270−3285

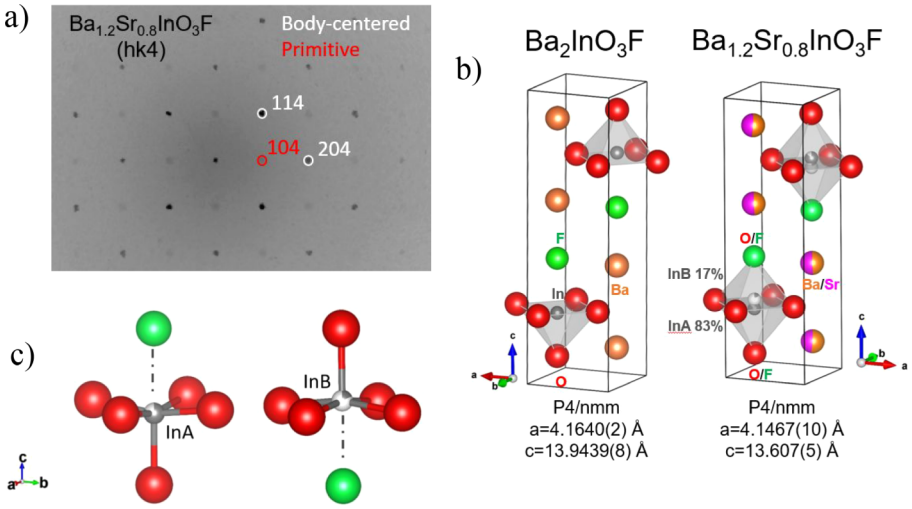

Figure 1. a) Identification of the primitive mode for SC-$Ba_{1.22}Sr_{0.78}InO_{3-y}F_{1-z}$ through indexation of reflections from single-crystal diffraction. b) $Ba_{1.2}Sr_{0.8}InO_{3-y}F_{1-z}$ structure, as compared to the Ba_2InO_3F network (data extracted from Needs & Weller[24]) with indium environment, occupancies (InA/InB), and unit cell parameters. c) Representation of InA and InB crystallographic sites, revealing distorted octahedra. The O (red spheres) and F sites (green spheres) are reversed between the $In(A)O_5F$ and $In(B)O_5F$ distorted octahedra.

Synchrotron SOLEIL, with λ = 0.51459 Å and a counting time of 9 s per step using a DECTRIS MYTHEN2 detector. Both sets of data were then refined using the Jana 2006 software,[37] with absorption correction = 0.73 (cylindrical sample, no preferential orientation).

2.3. Single-Crystal Harvesting

The grains of roughly ground powder previously set aside under argon were placed on a glass microscope slide in a drop of mineral oil to protect them from ambient humidity. Single crystals with diameter 20−50 μm were then identified and handpicked using a polarized light microscope and polymer-tipped micromounts.

2.4. Single-Crystal X-ray Diffraction

Single-crystal diffraction data were captured at room temperature for all samples using a Bruker KAPPA APEX II diffractometer with a Mo radiation source (λ = 0.71073 Å). APEX 4 software suite[38] was used for indexing and data reduction work. Olex2 software[39] was used, and the crystal structure was solved with the SHELXT[40] program and intrinsic phasing. The structure refinement was done using SHELXL[41] and a least-squares minimization. In the interest of clarity, for data extracted through single-crystal XRD, the exact stoichiometric coefficients obtained through XRD will be presented alongside the "SC" prefix when needed. For data collected on powders (P), the prefix "P" will be used when relevant, and the stoichiometric coefficients will reflect the proportions introduced during synthesis.

2.5. ^{19}F Solid-State Nuclear Magnetic Resonance

^{19}F solid-state nuclear magnetic resonance (NMR) experiments were performed under magic angle spinning (MAS) conditions with a Bruker Avance III 300 WB spectrometer (B_0 = 7.05 T, ^{19}F Larmor frequency of 282.4 MHz) equipped with a BL2.5 DVT X-H/F MAS probe and a BCU II Smart Cooler. The NMR spectra were recorded at various temperatures using a rotor-synchronized Hahn echo (π/2-τ-π) pulse sequence with a π/2 pulse length of 2.0 μs, a 30 kHz MAS rate (τ° = 30.33 μs), and an optimized recycle delay (from 10 to 30 s depending on the analyzed sample and the temperature). The temperature inside the rotor spinning at 30 kHz was estimated with KBr powder following the work of Thurber and Tycko.[42] ^{19}F NMR shift scale was calibrated using an external solid reference of KBF_4 (δ_{iso} = −153.3 ppm). Acquired NMR data were processed with Bruker TopSpin 3.6.1 software and analyzed as the sum of distinct resonance lines with the Dmfit program.[43]

2.6. Luminescence Measurements

Room temperature luminescence spectra were collected using a Horiba Jobin Yvon Fluorolog 3 spectrofluorometer equipped with a xenon lamp. The samples were all measured in powder form and placed in a sample holder small enough to guarantee that an equal volume of powder was measured for each sample to allow for proper comparison of luminescence intensity between samples. For 10K luminescence measurements, the powdered $Ba_{1.2}Sr_{0.8}InO_3F$ was placed inside a transparent sample holder cooled by liquid helium. Data collection was conducted by introducing the sample holder cell into the chamber. UV−vis absorption data were acquired from 200 to 800 nm using an Agilent Cary 5000, equipped with an integrating sphere. Data were plotted using the Kubelka−Munk function $F(R) = (1\text{-}R)^2/2R$, where R is the diffuse reflectance.[44] The Tauc plot $(F(R).h\nu)^{1/2} = B(h\nu\text{-}E_g)$ representing indirect transition band gap allows fitting the E_g band gap value.

2.7. Fluorine Titration

A solution was first prepared starting with 0.036 g of $Ba_{1+x}Sr_{1-x}InO_{3-y}F_{1-z}$ powder, dissolved in an aqua regia solution made from 3 mL of HNO_3 and 5 mL of HCl, and completed to 50 mL with ultrapure H_2O. The fluorine content in $Ba_{2-x}Sr_xInO_3F$ was estimated using a Mettler Toledo PerfectIon specific electrode. This solution was also used for the determination of cation molar percentages by ICP (Inductively Coupled Plasma).

2.8. Density Functional Theory (DFT) Calculations

A first set of calculations using the HSE06 Hartree-Fock/DFT hybrid functional[45,46] was performed with the ordered Ba_2InO_3F and $BaSrInO_3F$ structural models in order to get the most accurate band gap (in nature and magnitude) and density of states (DOS). The composition of the unit cell was $Ba_4In_2O_6F_2$ and $Ba_2Sr_2InO_6F_2$ (considering full ordering of Ba and Sr in both the 2*c* alkaline-earth sites, as well as the apical sites of O1 and F were fully occupied), where the lattice parameters were fixed to the experimental values obtained from the single-crystal analysis. In a second set of calculations, oxygen and fluorine vacancies were introduced on apical sites, thus involving supercells (compositions $Ba_8Sr_8In_8O_{23}F_8$ and $Ba_8Sr_8In_8O_{24}F_{62}$) as well as relaxation of atomic positions in the vicinity of the defects. As the HSE06 hybrid scheme became thus computationally overexpensive, the generalized gradient approximation (GGA, according to the Perdew, Burke, and Ernzerhof formulation[47]) was used for the exchange-correlation functional. By comparing results from GGA vs HSE06 for the systems without vacancies, we verified that only the magnitude of the band gap was affected, while other features of the electronic structure (density of states, energy dispersion, and electron density) were essentially unchanged. Monkhorst-type Brillouin zone samplings of 5 × 5 × 3 k-

https://doi.org/10.1021/acs.inorgchem.5c04288
Inorg. Chem. 2026, 65, 3270−3285

points were used. The plane-wave energy cutoff was 250 eV. The self-consistency criteria were 10^{-3} eV per cell for electronic convergence and 10^{-2} eV/Å for forces in structural optimizations.

Finally, the oxygen and fluorine vacancy formation energies were calculated using the PyDEF 2.0 program,[48] as well as the energy levels associated with oxygen and fluorine defects within the band gap. Since the chemical potentials of O^{2-} and F^- anions are clearly different, the formation energy values of the defects could only be compared two by two, by considering the oxygen vacancies on the one hand and the fluorine vacancies on the other hand, for Ba_2InO_3F and $BaSrInO_3F$.

3. RESULTS AND DISCUSSION

3.1. Structure Determination by Single-Crystal and Powder XRD Analysis

3.1.1. Indium Site Distribution and Anionic Disordering in the $Ba_{2-x}Sr_xInO_{3-y}F_{1-z}$ Network. The structures of the $Ba_{2-x}Sr_xInO_{3-y}F_{1-z}$ compounds were determined through single-crystal XRD measurements for all x values considered in this study. Figure 1a displays the partial reconstruction of the reciprocal space with a precession frame of the (hk4) plane, where the presence of weak peaks (circled in red) excludes any centering. Further careful examination of the systematic absences in the diffraction data set led to the determination of space group $P4/nmm$ ($P4/n\ 2_1/m\ 2/m$, n°129) for $Ba_{2-x}Sr_xInO_{3-y}F_{1-z}$ throughout the solid solution range, the same as for the parent Ba_2InO_3F phase. The crystal structure refinement showed an electron density residue of 6 e/Å^{-3} straight along the c axis, 0.70 Å away from the initial In site, in the center of the octahedron (Figure 1-b).

To account for this, two randomly occupied In positions were considered and called InA and InB (Figure 1c). This visibly improved the agreement factors of the refinement (from R_1 = 3.74% and wR_2 = 7.37% with only one In position to R_1 = 2.13% and wR_2 = 3.85% with two In positions). Occupancies for these two indium sites were refined at 83% for InA and 17% for InB in SC-$Ba_{1.22}Sr_{0.78}InO_{3-y}F_{1-z}$, which is the composition within the solid solution with maximal occupancy for InB (Table S1). For the other single crystals, occupancies vary slightly throughout the solid solution, but InA always exceeds 80% occupation (Table 1). Furthermore, the annealing under air of $BaSrInO_{3-y}F_{1-z}$ allows for a slight reduction in InB occupancy, changing from 15% to 10%. Additionally, the InB occupancy also drops significantly to 8% for the lowest Sr content synthesized, in SC-$Ba_{1.55}Sr_{0.45}InO_{3-y}F_{1-z}$. Complete structural data for all studied compositions within the solid solution are available in the Supporting Information (Tables S1−S4).

Table 1. Site Occupancy of the Split InA/InB Site for Different Compositions and Considering Various Annealing Atmospheres in the SC-$Ba_{2-x}Sr_xInO_{3-y}F_{1-z}$ Solid Solution Using Single-Crystal X-ray Diffraction Data

x	0.45(4)	0.66(2)	0.78(2)	1.00(2)	1.00(2)
Atm.	Ar	Ar	Ar	Ar	Dry air
InA	0.92(1)	0.85(2)	0.83(2)	0.85(2)	0.90(1)
InB	0.08(1)	0.15(2)	0.17(2)	0.15(2)	0.10(1)

Unlike the parent phase Ba_2InO_3F, where O and F atoms of the In octahedron are well ordered in the apical sites, the occurrence of two InA and InB sites is the signature of partial fluorine and oxygen anionic disorder between those apical sites with alternatively longer and shorter In−X bond lengths along the c-axis. Thus, the In^{3+} local environments shift from a square pyramid made out of O atoms in Ba_2InO_3F (Figure 1b,c) to an elongated octahedron, emphasizing O/F anionic disorder in the apical site with two kinds of In−X bond lengths in the $Ba_{2-x}Sr_xInO_{3-y}F_{1-z}$ solid solution. On the bond valence sum (BVS) calculation, discussed in Section 1.3, the larger In−X distance should correspond to X = F.

3.1.2. Evidence of Anionic Vacancies and In^+. Laboratory XRD acquisition was supplemented by synchrotron powder XRD measurements for a better estimation of the powder samples' homogeneity and possibly the presence of impurity phases (Figures S1 and S2). Rietveld refinement of synchrotron data used the structural model and the indium site distribution identified through single-crystal XRD analysis. It shows the presence of the expected $Ba_{2-x}Sr_xInO_3F$ composition, as well as minor impurities such as $(Ba,Sr)F_2$ ($Fm\bar{3}m$) and $SrIn_2O_4$ ($Pnam$) compounds. The final refinement of the P−$Ba_{1.4}Sr_{0.6}InO_{3-y}F_{1-z}$ composition is shown in Figure 2a.

Comparison of the diffraction data for all compositions shows a monotonic decrease of the c parameter and unit cell volume versus Sr rate in the $Ba_{2-x}Sr_xInO_{3-y}F_{1-z}$ phases (Figures 2b and S3 and Table S2). Attempts to synthesize compositions richer in Sr with $x \geq 1.0$, like $Sr_{1.2}Ba_{0.8}InO_3F$, were indeed unsuccessful and only led to the formation of more $SrIn_2O_4$ compound. Because Sr^{2+} has a smaller ionic radius than Ba^{2+}, increasing the Sr content in the phase contributes to an increase in InA/InB disorder in connection with anionic disorder and may lead to a phase demixion.

Samples were annealed in parallel at 1050 °C, both under Ar and dry air atmospheres. A comparison of the resulting powder XRD patterns is presented in Figure 2c for P−$Ba_{1.2}Sr_{0.8}InO_{3-y}F_{1-z}$ as an example. The first observation that can be done is a noticeable unit cell volume reduction after the dry air annealing as the diffraction peaks shift toward higher angles. The second point is peak intensity variation as shown here with the I_{103}/I_{110} ratio inversion, possibly linked to preferred orientations but also to modified structure factors. Single-crystal structure analysis already showed a lower anionic disorder in the dry air-annealed samples as the main InA-site occupancy increased (Table S4). All of these observations could be explained by the presence of In^+ in the argon-synthesized compound in relation to a significant amount of anionic vacancies. These could be filled by oxide anions during the dry air treatment, thus, oxidizing In^+ into In^{3+}. Another hypothesis should be to consider the following anionic stoichiometry, $O_{3+x}F_{1-2x}\blacksquare_x$ containing x anionic vacancies and only In^{3+}. However, to keep the electroneutrality, if an oxygen substitution for fluorine occurs during the annealing under air, it leads to a increase in the vacancy rate and an increase of unit cell parameters should be observed, which is not the case. The only way to explain a decrease of unit cell parameters after annealing under air is to consider an oxidation phenomenon $In^+ \rightarrow In^{3+}$ and a reduction of anionic vacancy rate.

Unit cell parameter variation can be a good indication of the In^+/In^{3+} partial occupancy. In^+ exhibits a larger ionic radius $r(In^+)$ than In^{3+} ($r(In^{3+})$ = 0.8 Å, 6-fold coordinated to oxygen[49]) due to its lone pair. Five In^+-X^- bond lengths can be found in InBr (1 apical In−Br = 3.024 Å + 4 equatorial In−Br = 3.295 Å[34]) or InCl (1 apical In−Br = 2.839 Å + 4 equatorial In−Cl = 3.205 Å[33]), both crystallizing in the $Cmcm$ space group. Taking into account that $r(Br^-(VI))$ = 1.96 Å[49] and $r(Cl^-(VI))$ = 1.81 Å[49], the deduced $r(In^+)$ can be estimated at

https://doi.org/10.1021/acs.inorgchem.5c04288
Inorg. Chem. 2026, 65, 3270−3285

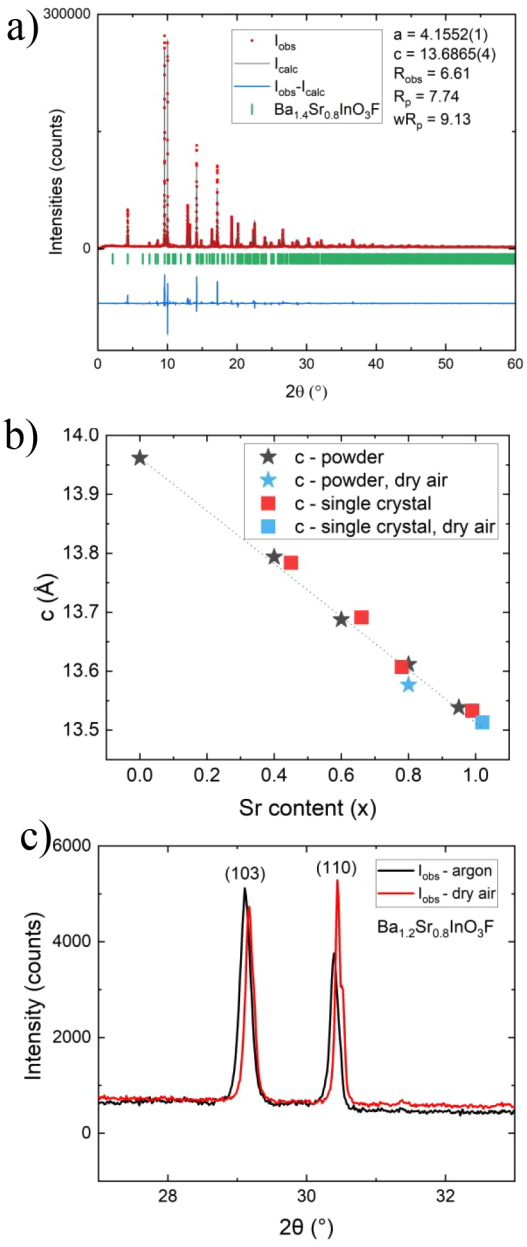

Figure 2. a) Rietveld refinement of powder X-ray diffraction data of P−$Ba_{1.4}Sr_{0.6}InO_{3-y}F_{1-z}$. Data acquired at Synchrotron Soleil, Beamline CRISTAL, λ = 0.514 Å. b) Evolution of the c lattice parameter as a function of Sr content, extracted from powder and single-crystal XRD data, with standard deviation. Dry air-annealed samples are represented next to as-synthesized samples (Ar annealing). A line is drawn as a guide to the eye. The lattice volume values follow the same trend (Figure 3-SI). c) Evolution of powder XRD diagram (λ= 1.5418 Å, enlargement 27.5°< 2θ < 32.5°) of P−$Ba_{1.2}Sr_{0.8}InO_{3-y}F_{1-z}$ annealed under Ar and dry air (change of intensity ratio and volume decrease after dry air annealing).

around 1.335−1.395 Å for the equatorial plane. A simple calculation then shows that the presence of 5% In^+ should lead to a 1% increase of the unit cell parameter. Indeed, assuming an ionic radius of 1.36 Å for In^+, a linear combination of 95% In^{3+} (0.80 Å) and 5% In^+ (1.36 Å) leads to an average ionic radius of 0.828 Å, corresponding to a theoretical parameter a = 2d(In−O) = 4.456 Å instead of 4.40 Å for the theoretical parameter of a structure containing only In^{3+}. A variation of a parameter around 1% is indeed expected.

For example, $\Delta a/a = 2.10^{-3}$ in the case of P−$Ba_{1.2}Sr_{0.8}InO_{3-y}F_{1-z}$ (powder XRD data, Table S2). The c unit cell parameter should also be affected by the In^+ presence because of the lone pair hindrance. Anionic vacancies located in the apical O/F site at longer bond lengths from In^+ will indeed help to pull the perovskite layers apart by Coulombic repulsion directly related to the lone pair ($5s^2$). Thus, the c unit cell parameter is going to increase when dry air is replaced by Ar-atmosphere annealing: $\Delta c/c = 2.10^{-3}$ for P-$Ba_{1.2}Sr_{0.8}InO_{3-y}F_{1-z}$ (Table S2).

The In^+ ion would then sit in a C_{4v} point group symmetry site, with the square pyramid formed by the four equatorial O and one apical anion (O or F), and a vacancy occupied by the lone pair ($5s^2$) in place of the sixth anion in the octahedron.

In order to conclude about the occurrence of anionic vacancies after annealing under Ar, atomic ratios were confirmed by inductively coupled plasma spectroscopy (ICP) and fluorine-specific electrodes after sample dissolution. ICP measurements performed on the Ar-treated P−$Ba_{1.2}Sr_{0.8}InO_{3-y}F_{1-z}$ sample showed cationic ratios closely aligning with the expected values (Ba1.20(1) Sr0.84(1) In1.04(1)). The slight excess of In and Sr could be explained by the presence of the $SrIn_2O_4$ phase as an impurity. Fluorine titration performed with an F^- specific electrode on the same solution showed a fluorine stoichiometric coefficient of 0.94(1). The measurement was repeated three consecutive times for accuracy and yielded the same value every time. However, when taking into account the small amount of impurity (3% of $SrIn_2O_4$ at least, deduced from the Rietveld refinement), it is difficult to reach conclusions about the possible stabilization of anionic vacancies when solely using data from chemical analysis. Taking into account all these considerations, it is reasonable to consider

3.1.3. Evolution of Bond Lengths, Bond Angles, and Bond Valence. Concerning the InA and InB site occupancies, as mentioned previously in part 1.1, the maximum InB site occupancy is equal to 17% in the SC-$Ba_{1.22}Sr_{0.78}InO_{3-y}F_{1-z}$ composition, inducing anionic disorder. On the other hand, Ba^{2+} and Sr^{2+} ions are randomly distributed over the 2c Wyckoff positions and the occupancies vary in agreement with the chemical formulas (Table 2).

Such a distribution between larger and smaller polarizable cations may also affect the location of anions in the apical sites of the InO_5F octahedra. Interatomic distances and bond angles calculated from single-crystal X-ray diffraction data of $Ba_{2-x}Sr_xInO_{3-y}F_{1-z}$ with varying values of x and for different atmospheres applied during thermal treatment were reported in Tables S1−S4. The Ba/Sr2 ionic site remains larger (synonymous with lower BVS) than the Ba/Sr1 site, whatever the Sr content (Table 2), but this difference in size (or in BVS) between the two sites visibly decreases as the Sr amount increases. It has to be emphasized that the $Ba_{1.2}Sr_{0.8}InO_{3-y}F_{1-z}$ composition showcases the closest valence values for the two (Ba/Sr) sites, despite the difference in ionic size and in proportions between Ba^{2+} and Sr^{2+}. For this composition, the similarity in terms of size and valence of the two alkaline-earth sites on either side of the perovskite layers highlights the disorder linked to the two alkaline-earths, the two indium sites, and finally both the anions occupying the apical sites.

The examination of the atomic displacement parameters shows that they are almost isotropic for all Ba/Sr and InA/InB cations and significantly anisotropic for anions. Moreover, the anisotropy of the O2 anions in the equatorial plane of the

https://doi.org/10.1021/acs.inorgchem.5c04288
Inorg. Chem. 2026, 65, 3270−3285

Table 2. Ba/Sr Site Occupancy and Bond Valence Sum (BVS), Extracted and Calculated from Single-Crystal XRD Data[a]

x	0	0.45(4)	0.66(2)	0.78(2)	1.00(2)	1.00(2)
Atm.	Ar	Ar	Ar	Ar	Ar	Dry air
Occupancies						
Ba1	1	0.777(2)	0.66(2)	0.58(2)	0.48(2)	0.448(2)
Sr1	0	0.22(2)	0.34(3)	0.42(2)	0.52(3)	0.55(2)
Ba2	1	0.776(2)	0.68(2)	0.62(2)	0.53(2)	0.539(2)
Sr2	0	0.22(2)	0.32(3)	0.38(2)	0.47(3)	0.46(2)
Valences (V)						
V1= Ba/Sr1	1.984	1.898	1.780	1.725	1.695	1.789
V2 = Ba/Sr2	1.686	1.643	1.661	1.673	1.597	1.595
V1−V2	0.298	0.255	0.119	0.052	0.098	0.194

[a]For each Sr content, the unit cell parameters, the Ba/Sr1 and Ba/Sr2 atomic positions, and the deduced Ba/Sr-X (O,F)bond lengths are reported in Tables S1−S4. Considering the In−X apical distance, the longest one is systematically attributed to fluorine atoms for the BVS calculation for all ions .

InO_5F distorted octahedra is along the *c* axis, while that of the apical O1 and F sites is in the basal plane of the unit cell (Figure 3a). However, the estimated standard deviation (ESD) of atomic displacement parameters (ADP) of anions remains rather high. Because of a large content of heavy atoms (Ba, Sr, and In), the electron density map is dominated by them, which limits the observation of light elements like fluorine and oxygen. Moreover, the XRD data were recorded at room temperature. These first observations are followed by a careful analysis of the bond lengths and bond angles along the solid solution.

Regarding the In−O/F apical bond lengths (Figure 3b), the long In−F bond becomes shorter, and the short In−O1 bond appears longer with increasing Sr content. An almost similar evolution is seen for InB (Table S3), with the inverted O1 and F bonds to maintain a longer bond length for InB-F than for InB-O1. Then, the InB-O1 bond length does not show significant variation with increasing Sr rate, whereas the InB-F bond lengths decrease less strongly than the InA-F ones (Table S3). In the equatorial plane, the InA/B−O2 bond lengths slightly decrease from 2.11 to 2.08 Å between Ba_2InO_3F and $BaSrInO_3F$.

The evolution of the O2−In(A/B)-O2 bond angles between the indium sites and each of the diagonally opposite equatorial O2 atoms shows that the $In(A/B)O_4$ square pyramids are flattened as the Sr content increases (Figure 3c). The InB site is also closer to a 180° planar configuration compared to the InA site, with a maximum of 170.4° reached for O2-InB-O2 for x = 0.80. One should outline that in the literature, lower angles around 161° and 162° are detected in InCl[33] and InBr[34] (*Cmcm*), respectively, where monovalent indium is stabilized.

The higher this angle in the equatorial plane, the stronger the hybridization between the $4d^{10}5s^2/5s^0$ (In) orbitals and the 2p(O) orbitals of the equatorial O atoms, leading to an increase in the In−O bond covalency. However, with increasing Sr content, the spacing of the (Ba,Sr)(O,F) rocksalt layers decreases, and consequently, so does the ionic character of the A−X (A = Ba, Sr; X= O,F) bond length. In turn, through inductive effects, this is expected to decrease the $In\text{-}(O/F)_{apical}$ bond covalency in the perovskite layers, leading to a probable increase of the O/F ionic mobility in the apical site. This strong In(4d)-O(2p) orbital overlapping in the basal plane (with σ character) contributes to destabilizing the $\sigma(x^2\text{-}y^2)$ bands near the Fermi level while stabilizing the $\sigma(z^2)$ orbitals. It should allow for the expression of the $5s^2$ (In^+) lone pair, which is going to develop in place of the anionic vacancy. In

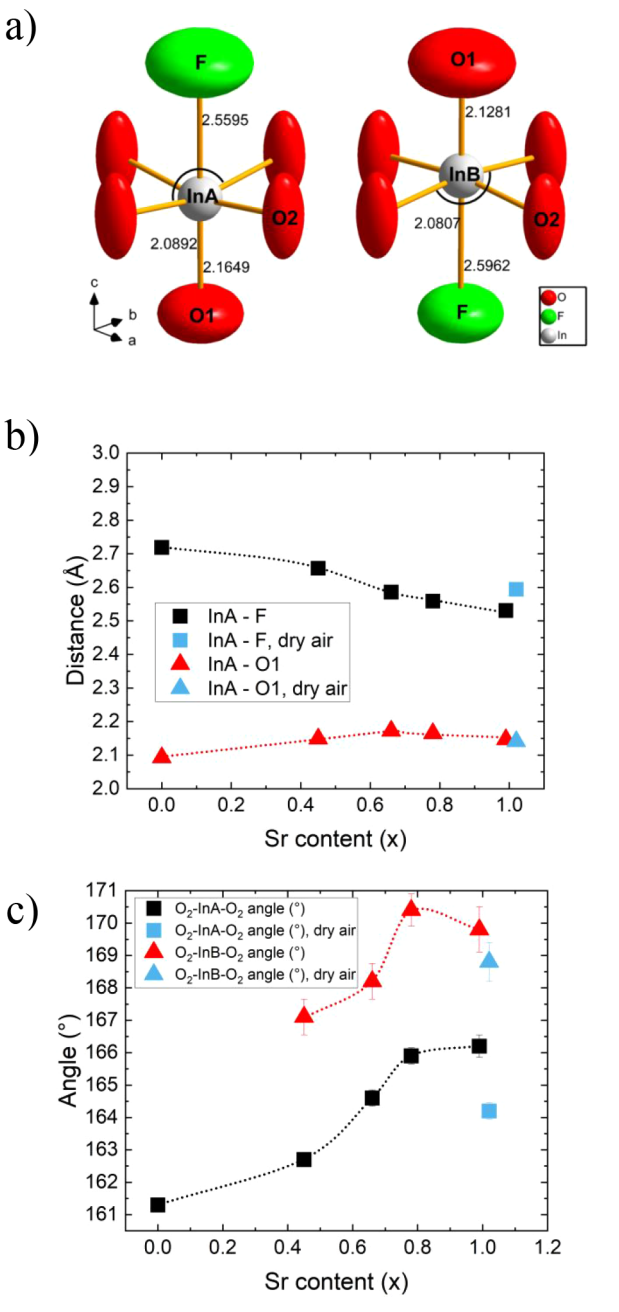

Figure 3. a) Local environment of the two In sites InA and InB.

https://doi.org/10.1021/acs.inorgchem.5c04288
Inorg. Chem. 2026, 65, 3270−3285

summary, the distorted InO_5F octahedra evolve into a more symmetric one with higher orbital overlapping in the equatorial plane. Then, the probability of observing an O/F anionic disorder in the apical sites should increase with higher Sr content. The most relevant difference between the InA and InB sites concerns the O2−In−O2 bond angles in the equatorial plane. It should come from the stabilization of a $5s^2$ electron doublet. Because a lone pair along the *c* axis has stronger Coulombic repulsive forces than the bonded groups in the equatorial plane, monovalent indium ($5s^2$) should preferentially occupy the InB site. However, this InB site cannot be fully occupied by monovalent indium because the In^+ content is probably rather small on the basis of previous considerations. Indeed, the O2−InB−O2 bond reached an optimum value for the SC-$Ba_{1.22}Sr_{0.78}InO_{3-y}F_{1-z}$ composition. Finally, one should emphasize that the InB site occupancy decreases after annealing under dry air, as a consequence of the depletion in In^+.

The anionic disorder related to the apical sites of the InO_5F octahedra can be emphasized through a bond valence sum (BVS) analysis (Figure 4 and Table S5).

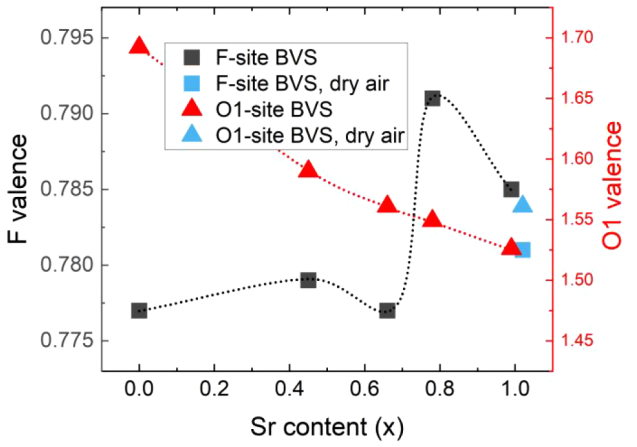

Figure 4. BVS of apical anions (O1 vs F) around the In sites. Lines are drawn as a guide to the eye.

It shows a large decrease in O1-site BVS (from 1.692 in Ba_2InO_3F to 1.526 in $BaSrInO_{3-y}F_{1-z}$), whereas the F site BVS slightly increases (from 0.777 in Ba_2InO_3F to 0.791 in $Ba_{1.2}Sr_{0.8}InO_{3-y}F_{1-z}$) along with Sr content. For the SC-$BaSrInO_{3-y}F_{1-z}$ composition annealed under air, the increase in BVS linked to the O1 site (from 1.526 under Ar to 1.561 under air) and the slight decrease in BVS related to the F site (from 0.785 under Ar to 0.781 under air) illustrate the reduction in anionic disorder, in agreement with the increase in InA occupancy from 85% to 90%. On the basis of BVS calculation, it is well known in oxyfluorides that In−F bonds should be longer than In−O bonds, as is for instance observed in ReOF[50,51] (Re: rare earth) compounds or in the parent phase Ba_2InO_3F[21], thus creating anionic disorder in the $Ba_{2-x}Sr_xInO_3F$ series. The BVS (Table S5) for InA and InB sites remains almost identical and slightly increases with the Sr content. This type of MO_5X distorted octahedra in layered perovskites was reported for other similar *P*4/*nmm* or *I*4/*mmm* compounds in the literature.[24,28,31,36,52,53] In these examples, the octahedron can sometimes exhibit anionic disorder involving apical sites, which could give rise to ionic mobility involving O^{2-}, F^-, Cl^-, H^+ (OH^-) or lead to spin crossover in the case of Co(III).

The BVS of the F-site increases and passes through a maximum at x = 0.8, whereas the O valence decreases regularly versus Sr content. Such evolutions should illustrate the atomic disorder.

To delve further into the details of the fluorine local environment and mobility in $Ba_{2-x}Sr_xInO_3F$, ^{19}F MAS NMR spectroscopy is used to investigate order/disorder and bonding in these compounds.

3.2. ^{19}F MAS NMR Investigation, F Local Environment, and Mobility

The ^{19}F MAS NMR spectra of $Ba_{2-x}Sr_xInO_{3-y}F_{1-z}$ are shown in Figures 5-a and S4. These spectra exhibit particularly broad resonance lines arising from Ba/Sr local disorder, as well as the partial InA/InB distribution around F atoms. Three main components can be used to reconstruct the ^{19}F MAS NMR spectra (Figure S4). For BaF_2 and SrF_2 fluorite-type structures where fluorine atoms are located in the tetrahedral sites of an alkaline earth lattice, the observed NMR ^{19}F signals are characterized by isotropic chemical shifts at −14.3 ppm and −87.5 ppm, respectively.[54] In the Ruddlesden−Popper (n = 1) phase, fluorine atoms are located in the apical position in the indium polyhedra and are surrounded by five Ba/Sr alkaline earths and one In, forming a distorted octahedral site, as represented in Figure 5c. Furthermore, the 4 F−Ba/Sr1 bond lengths in the basal plane remain almost identical around 3.00 Å versus Sr content, whereas the one apical F−Ba/Sr1 distances strongly decrease from 2.68 to 2.51 Å as the Sr rate increases (Figure 5d and Table S3). Furthermore, the apical F−In bond length strongly decreases from 2.72 Å in Ba_2InO_3F to 2.53 Å in $BaSrInO_3F$ (Table S3). Of the six bond lengths around F^- ions, only two are significantly affected by the presence of strontium. Thus, depending on the nature of the alkaline earth ion (Ba/Sr) and the F−Ba/Sr/In bond lengths, chemical shifts will vary. Then, the resonance lines with chemical shifts close to −60 and −90 ppm may be associated with Ba-rich and Sr-rich F local environments, respectively, and the third component with intermediate chemical shift would be consistent with a mixed Ba/Sr site. In other words, the Ba-rich component should correspond to FBa_5In and FBa_4SrIn local environments, the mixed Ba/Sr resonance line to FBa_3Sr_2In and FBa_2Sr_3In local environments, and finally the Sr-rich component to the $FBaSr_4In$ and FSr_5In sites. From $BaSrInO_{3-y}F_{1-z}$ to $Ba_{1.4}Sr_{0.6}InO_{3-y}F_{1-z}$ compositions, the intensity of the peak linked to the Ba-rich contribution increases, whereas the Sr-rich one clearly decreases, in accordance with the Ba/Sr ratios in the compounds. It should be pointed out that the intensity of the intermediate resonance line (corresponding to the mixed Ba/Sr environment) is maximum for x = 0.8. As previously underlined for this specific composition, the two (Ba/Sr) sites exhibit the closest BVS (Table 2), which is associated with a similar ionic size on each side of the two perovskite layers. The two alkaline earth sites with the *P*4/*nmm* structural hypothesis become almost identical in average size, whereas in the case of the parent phase containing only Ba, the two BVS specific to Ba^{2+} ions are very different (Table 2). This evolution of the BVS of the Ba/Sr sites with the Sr ratio could therefore reflect anionic disorder at the apical sites of the In^{3+} octahedron. It is indeed interesting to note, for instance, that in the case of the K_2NbO_3F oxyfluoride crystallizing with the *I*4/*mmm* space

https://doi.org/10.1021/acs.inorgchem.5c04288
Inorg. Chem. 2026, 65, 3270−3285

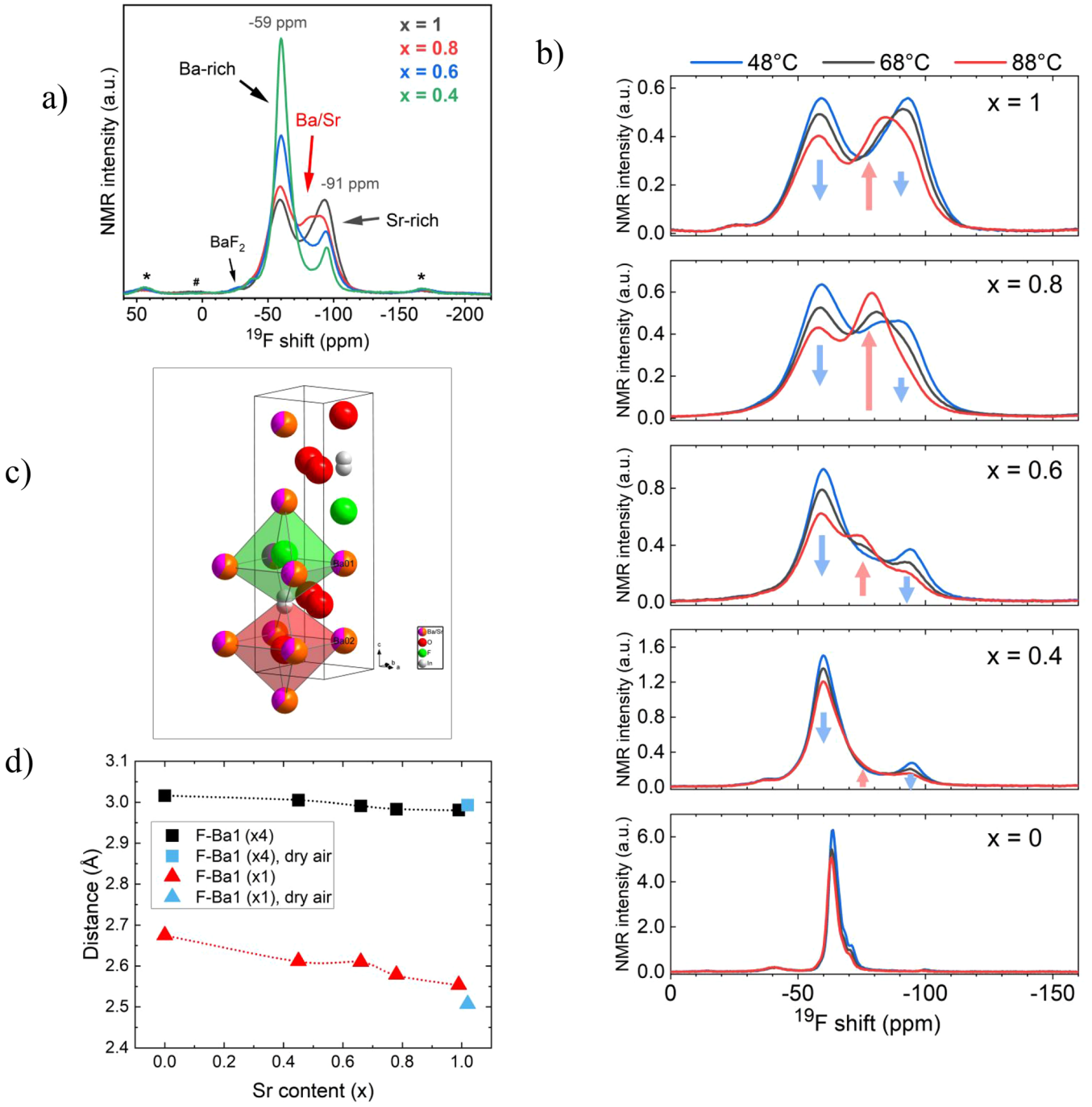

Figure 5. a) ^{19}F MAS NMR spectra (recorded at 48 °C with MAS rate 30 kHz, *,# spinning side bands) of P−$Ba_{2-x}Sr_xInO_{3-y}F_{1-z}$ showing the various F local environments. b) Effect of temperature on ^{19}F MAS NMR spectra (MAS rate 30 kHz) showing the strong change of F−In(Ba/Sr)$_5$ local environments depending on x-Sr content with the occurrence of fluorine vacancies and hopping phenomena, outlining the F mobility. c) Fluorine local environment in $Ba_{2-x}Sr_xInO_{3-y}F_{1-z}$ and d) representation of the F−Ba/Sr1 (4 + 1) bond lengths versus x-Sr content in $Ba_{2-x}Sr_xInO_{3-y}F_{1-z}$, extracted from single-crystal X-ray diffraction analysis.

group, only one site for the large polarizable cation (K, Sr, or Ba) is identified, accompanied by anionic disorder at the apical O/F site. Occurrence of anionic vacancies in the apical sites, stabilization of $In^+(5s^2)$ lone pair, and a larger extent of (O/F) anionic disorder were jointly underlined for this phase. In order to probe the fluorine mobility in this series, ^{19}F MAS NMR spectra were recorded at various temperatures and reported in Figure 5b.

The Ba_2InO_3F MAS NMR spectrum can be reconstructed with three narrow lines with chemical shifts ranging from −60 to −70 ppm, indicating various F local environments probably related to unexpected disorder involving (O1/F) apical sites (Figure S4).^{19}F NMR is a local probe, while XRD gives an average signature of the structure. The occurrence of a main NMR resonance with two additional peaks at lower chemical shifts means that distorted octahedra (with five Ba^{2+} and one In^{3+} on vertices) hosting the fluorine atom are locally slightly different with various bond lengths. The slight decrease of intensities with increasing temperature for all NMR lines in Ba_2InO_3F reflects a change (shortening) in spin−spin

https://doi.org/10.1021/acs.inorgchem.5c04288
Inorg. Chem. 2026, 65, 3270−3285

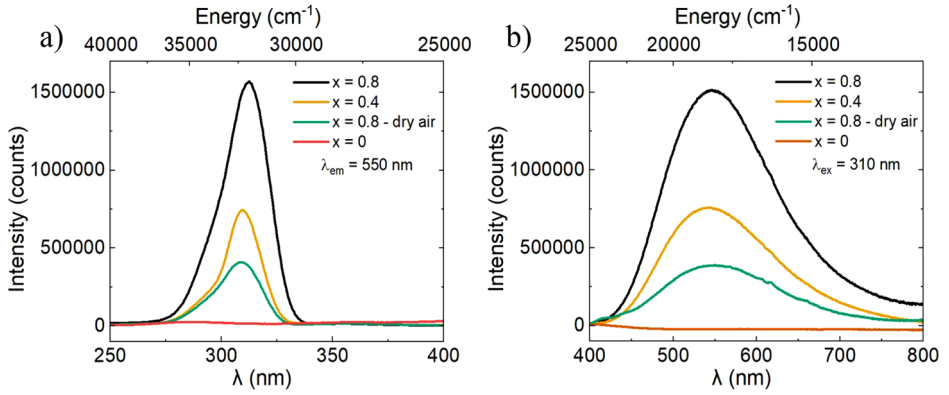

Figure 6. a) Excitation and b) emission spectra for varying strontium content x in P−Ba_2-xSrxInO_3F at room temperature.

relaxation time (T_2) that may affect the efficiency of the Hahn echo pulse sequence, especially when T_2 (or apparent T_2) becomes shorter or close to the interpulse delay (τ).[55] For the $Ba_{2-x}Sr_xInO_{3-y}F_{1-z}$ samples with $x > 0.5$, another phenomenon is clearly evidenced by the variable-temperature ^{19}F MAS NMR experiments. As the temperature inside the rotor increases, the intensity of both Ba-rich and Sr-rich resonance lines decreases in parallel with the growth of an intermediate NMR signal at about −80 ppm (Figures 5b and S4a). Actually, the evolution of the last component with temperature, clearly observed for the x = 0.8 compound, reflects the fluorine mobility favored by the presence of anionic vacancies on the (O1/F) site. It corresponds to a fluoride-ion exchange between two anionic sites, resulting in a decrease of the NMR signals associated with Ba-rich and Sr-rich F sites and the concomitant appearance of a resonance line with intermediate chemical shift (with a Ba/Sr atomic ratio close to 1)[56−58]

It is not possible to determine the proportions of each of these species grouped in pairs because the spin−spin relaxation times T2 differ, particularly between the Ba/Sr intermediate species and the two extremes. In Figure S4b, we have shown how the spectra evolve significantly with interpulse delay of Hahn echo sequences, particularly for the intermediate resonance, whose intensity drops dramatically, showing that the T2 time is shorter. This significant decrease in T2 is mainly associated with the progressive change of the first neighbor's nature (polarizability) as well as the variation of F−F distance. However, a clear break in T2 relaxation time appears for the intermediate Ba/Sr component, illustrating the presence of anionic vacancies that will force F^- ions to interact with other F- ions further away than 3.57 Å (Table S3). It is therefore this intermediate contribution, which increases with temperature, that is direct evidence of the presence of anionic vacancies as well as F^- ion mobility.

Thus, the variable-temperature ^{19}F MAS NMR experiments clearly evidenced a higher mobility of fluoride ions within the $Ba_{1.2}Sr_{0.8}InO_{3-y}F_{1-z}$ structure.

This result is consistent with the structural studies exposed in the previous subsections, in which this specific composition showed the following characteristics:

Two indium sites with the highest InB occupancy (17%).

Strong anionic disorder involving apical sites.

The orbital overlap involving In^{3+}/In^+ ($4d^{10}5s^0/5s^2$) and O ($2p^6$) in the basal plane is the greatest, with the largest O2-InA/B−O2 bond angles.

The two sites containing alkaline-earth ions are the closest in terms of ionic size and valence, indicating a homogeneous distribution of these highly polarizable cations.

To conclude on the anionic vacancies, a size discrepancy within a mixed (Ba/Sr) environment provokes steric constraints but also chemical pressure around Ba^{2+} that triggers anionic mobility through the creation of anionic vacancies located in disordered apical sites.

To conclude on the indium valence state, because of the presence of anionic vacancies around the specific InB local environment with a large increase in the number of O2−InB−O2 bond angles, the stabilization of the In^+ ($5s^2$) species seems obvious.

The impact of the ordering/disordering of the O1/F in apical sites as well as the anionic vacancies related to $In^+(5s^2)$ stabilization on the photoluminescence properties in this series was investigated from room temperature to T = 10 K.

3.3. Photoluminescence Properties

At room temperature, the photoluminescence properties, through excitation and emission spectra of the $Ba_{2-x}Sr_xInO_{3-y}F_{1-z}$ series, are illustrated in Figure 6a,b. It exhibits a broad emission band ranging from 450 to 750 nm under ultraviolet excitation at 310 nm. The corresponding intensity is visibly impacted by the Sr:Ba atomic ratio. Starting from the parent Ba_2InO_3F phase, the intensity varies in correlation with the Sr content, but the Sr/Ba molar ratio has no influence on the spectral distribution (Figure 6b). A maximum is reached for x = 0.8. Regardless of composition, the corresponding excitation curves display a maximum at 310 nm. The absorption band recorded at room temperature is constituted by at least two components, as a lower intensity band is clearly detected at higher energy (280 nm). In double Ce^{3+}-doped A_2KInF_6 (A= Rb, K, Na) perovskite networks reported by Chaminade et al.[59] and later by Cornu et al.[60] and Gaudon et al.[61] with In^+ located in a regular octahedral site engaging ionic bonds, the excitation band appears at 255 nm (4.9 eV).[61] In the present oxyfluorides with a layered perovskite structure where the In^+ ions are stabilized in square pyramids with four strong In−O covalent bonds, the absorption band is red-shifted to 310 nm. This redshift of the excitation bands is in accordance with the structural features, despite the additional influence of anionic vacancies in the Ruddlesden−Popper phase. Considering the structural features showing the stabilization of monovalent indium, the lack of two positive charges could be balanced by one oxygen

https://doi.org/10.1021/acs.inorgchem.5c04288
Inorg. Chem. 2026, 65, 3270−3285

or two fluorine vacancies. At this stage, several hypotheses could explain the radiative emission detected at room temperature. First, the stabilization of monovalent indium enables the observation of the $ns^2 \leftrightarrow ns^1np^1$ orbitals transition, which is well described for the ns^2 cation in the literature.[62,63] Second, the vacant anionic sites generate energetic levels within the band gap, which act as electron traps during the radiative process induced by ultraviolet irradiation. Indeed, ns^2 compounds have also been shown to exhibit luminescence through other mechanisms, such as self-trapped excitons, which might show a large emission band and Stokes shift.[64−66]

Complementary measurements were performed on the heat-treated powder (dry air atmosphere) previously mentioned. A significant drop in the intensity is observed (Figure 6b, green curve), meaning that the origin of the luminescence is linked to species with a concentration highly sensitive to the oxygen content. A similar thermal behavior was reported by Green et al. in the Ba_2SrGaO_4F oxyfluoride,[67] but the authors did not explain the origin of the luminescence. Consequently, these variations could be linked to the initial presence of anionic vacancies in the Ar-synthesized compound, which would be filled by the flow of oxygen in the dry air atmosphere, thus oxidizing In^+ back into In^{3+}.

Let us consider the first hypothesis: the sample annealed under Ar stabilizes the In^+ cation within the $Ba_{2-x}Sr_xInO_{3-y}F_{1-z}$ compound. Similar to other ns^2 compounds, such as Sb^{3+}, Bi^{3+}, Ga^{3+}, Sn^{2+}, and Pb^{2+}, monovalent indium might present a luminescence emission.[62] The energy diagram of the ns^2 lone-pair ions is constituted by the $^1S_0$ ground state and the ^3P_J (J = 0,1,2) excited states. The $^1S_0 \rightarrow {}^3P_1$ radiative absorption (more specifically $^1A_{1g} \rightarrow {}^3T_{1u}$ in an octahedral (O_h point group) crystal field) is generally observed. It is spin-forbidden[62] and labeled as A-band. The other transitions correspond to $^1S_0 \rightarrow {}^3P_2$ ($^1A_{1g} \rightarrow {}^3E_u + {}^3T_{2u}$), which is less intense and known as B-band, and to $^1S_0 \rightarrow {}^1P_1$ ($^1A_{1g} \rightarrow {}^1T_{1u}$), allowed by the spin (and parity) selection rule[62] and denoted as C-band,[68] appearing at higher energy. The radiative emission corresponding to the A-band is composed of two A_X and A_T sub-bands, related to Jahn−Teller coupling of the orbital triplet. The only transition authorized by the Laporte rule ($\Delta s = 0$, $\Delta l = 1$) is the $^1P_1 - {}^1S_0$ transition. However, through spin−orbit coupling,[69,70] the $^1S_0 - {}^3P_1$ transition is observed. The octahedral coordination of the monovalent Indium leads to a removal of the excited p level degeneracy. The resulting A_T and A_X emission bands correspond to the two minima of the adiabatic potential energy surface (APES) curve. This luminescence is generally strongly dependent on the temperature. At room temperature, irradiation causes a thermal depopulation of the highest potential well (A_T), in favor of the lowest energy minimum, A_X. Consequently, only the lowest energy band A_X is detected. Such an emission was fully described in alkali halogenide compounds.[61,71−73] The A_x-associated emission band covers part of the visible range, whereas the contribution of the A_T band is located in the ultraviolet. Because this $ns^1np^1 \leftrightarrow ns^2$ emission is strongly sensitive to the temperature, cooling to liquid Helium temperature can be necessary to detect both components.[59−61] The nature of the $ns^2 \leftrightarrow ns^1np^1$ radiative transition is confirmed in these last articles by the appearance of a unique excitation band at 255 nm and a thermal dependency of the A_x and A_T emission bands. These bands are associated with In^+ in a regular octahedral site involving In−F ionic bonds.

For this reason, the highest emitting composition (x = 0.8) was investigated at low temperatures (Figure 7a,b). In both

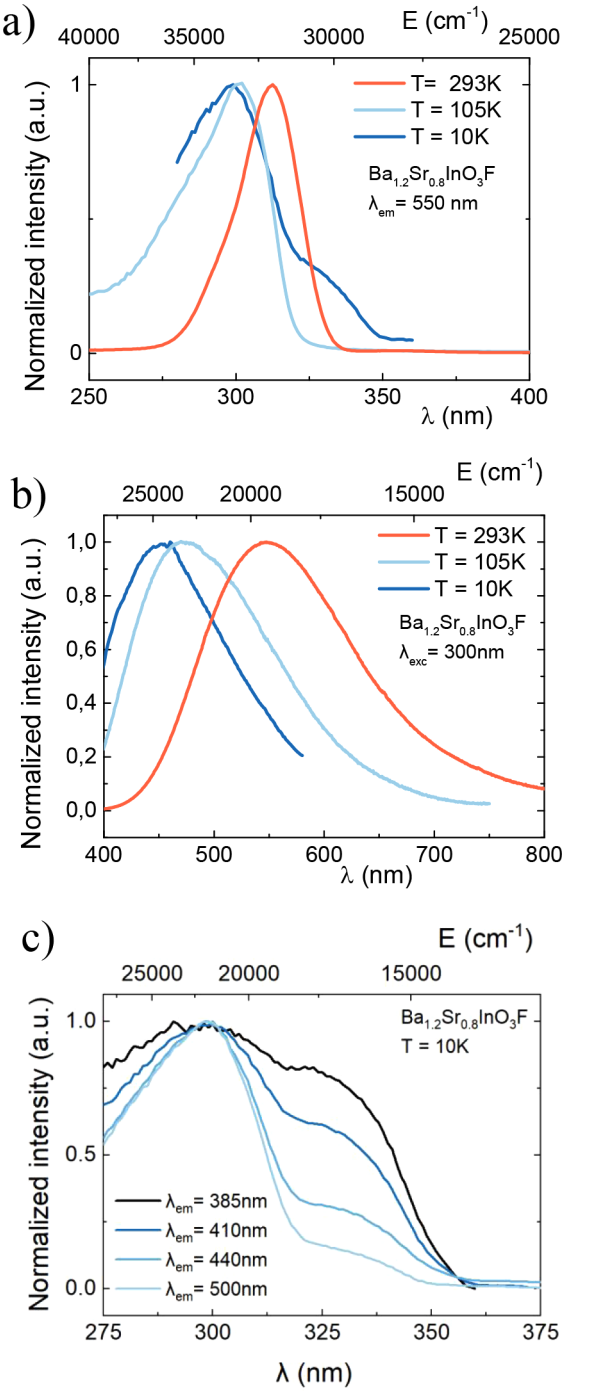

Figure 7. a, c) Normalized excitation and b) emission spectra of $Ba_{1.2}Sr_{0.8}InO_3F$ compositions at various temperatures.

excitation and emission curves, the bands are shifted toward higher energies than the ones observed at room temperature: from 315 nm (3.9 eV, RT) to 300 nm (4.13 eV, T = 105 K) for the excitation spectra and from 550 nm (RT) to 480 nm (T = 105 K) for the emission spectra. The blueshift with decreasing temperature follows with smaller coordination distances on average, causing a larger splitting between the s and p states and thus higher transition energies. At this stage, the discrimination between a potential A_T band in the UV-blue

https://doi.org/10.1021/acs.inorgchem.5c04288
Inorg. Chem. 2026, 65, 3270−3285

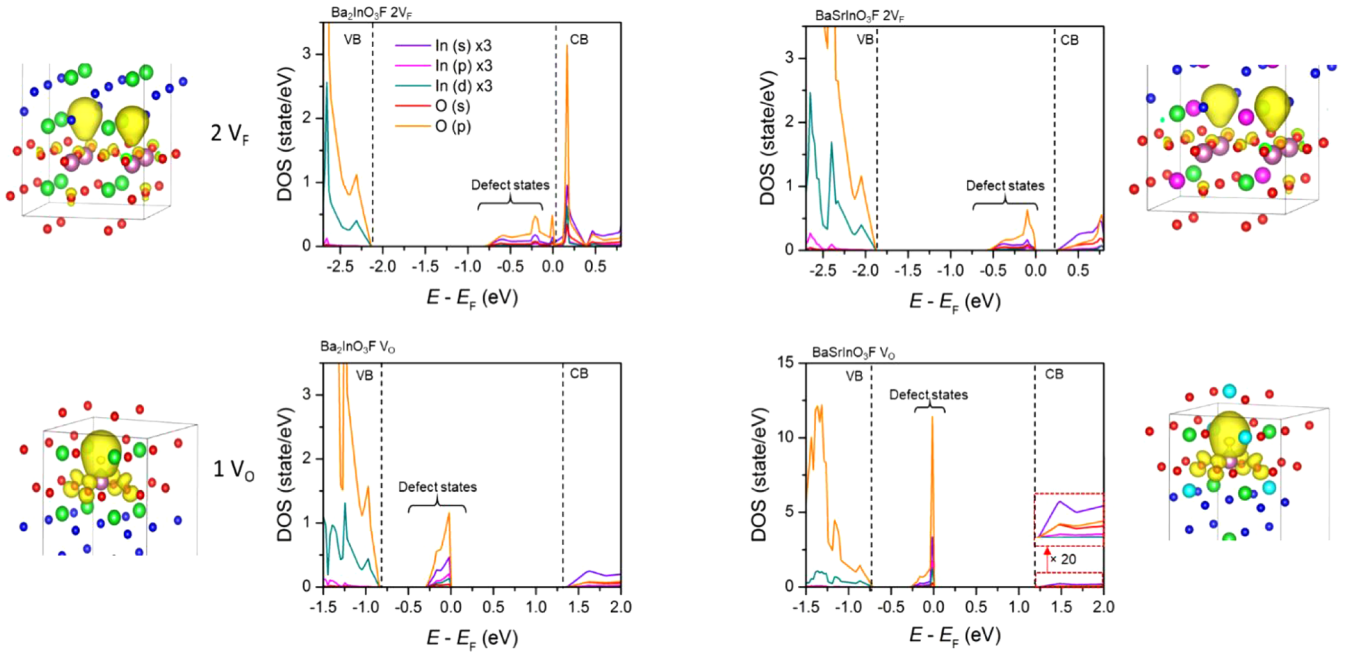

Figure 8. Representation of density of states (DOS) of Ba_2InO_3F with one oxygen vacancy 1 V_O (below, $Ba_{16}In_8O_{23}F_8$) or two fluorine vacancies 2 V_F (above, $Ba_{16}In_8O_{24}F_{62}$) and $BaSrInO_3F$ with one oxygen vacancy 1 V_O (below, $Ba_8Sr_8In_8O_{23}F_8$) or two fluorine vacancies 2 V_F (above, $Ba_8Sr_8In_8O_{24}F_{62}$) considering the various atomic positions and unit cell parameters, previously determined on the basis of single-crystal XRD analysis. The truncated unit cells were represented with the electron density (in yellow) representing the $5s^2$ (In^+) lone pair.

range and an A_x component at a lower energy is not possible. An attribution of the radiative process to a pure $ns^1np^1 \rightarrow ns^2$ transition of In^+ ions would suggest that the main part of the deexcitation process comes from the highest energy A_T band, meaning a significant quenching of the A_x one. In addition, the excitation curves reveal the appearance at 10 K of a second absorption band peaking at longer wavelengths (325 nm), whereas this contribution is not detected at T = 105 K (Figure S5). This implies that a new absorbing center is active at such a low temperature. Figure 7c clearly shows an increase in the relative absorption intensity between this new band and the one peaking at 300 nm when the fixed emission wavelength is shifted from 500 to 385 nm.

Taking these final observations into account, and given that an $ns^1np^1 \rightarrow ns^2$ electronic transition is highly sensitive to the crystal field and that no change in the spectral distribution is observed when the Sr/Ba molar ratio is varied, we cannot definitively conclude that the emission is purely an $ns^1np^1 \leftrightarrow ns^2$ transition of monovalent indium and completely exclude the contribution of defects to the radiative process observed at room temperature.

Consequently, we suggest that the emission observed at 10 K under excitation at 300 nm reflects the radiative transition of two types of emitting centers: a blue-green one excited at around 300 nm and a blue one excited at 330 nm (3.75 eV), which implies a smaller Stokes shift for this latter one. We propose a two-step mechanism. From room temperature down to T = 100 K, the blue-green emitting center is associated with the absorption band shifted from 310 to 300 nm. At T = 10K, an additional level is optically activated, and we can deduce that the apparent strong blue shift of the emission observed under the 300 nm excitation might be linked to the increased contribution of this new center together with a potential A_T band of In^+. Thus, the global emission is probably based on the coupling between the In^+ species and energetic levels related to the center detected at a low temperature. This last one should be linked to anionic vacancies.

Finally, taking into account the stronger increase of the O−In−O bond angle with Sr content from x = 0.4 to x = 0.8 (Figure 3c) and the resulting highest In−O bond covalency observed for x = 0.8, two hypotheses can be considered for the variation in intensity observed in Figure 6b. First, this could result from an optimized content of $In^+(5s^2)$ and associated anionic vacancies in specific $[InO_4F]^{8-}/[InO_5]^{9-}$units. Second, within a perovskite-layer network, the electronic delocalization is expected to occur when the O−M−O (M= metal) bond angles approach 180°. Moreover, the increase of the covalency in the basal plane, with almost linear O−In−O interactions, strongly promotes extended π bond formation. The electronic delocalization of the excited state might be associated with a broader bandwidth and a higher probability to populate the (STE) defects at the origin of the stronger emission observed at room temperature. This is illustrated by a widening of the excitation band and a lowering of its energy. Considering the investigated compound, this is reflected in the excitation spectra by a maximum intensity but also a slight redshift for the composition $Ba_{1.2}Sr_{0.8}InO_{3-y}F_{1-z}$ in which the O−In−O bond angle is the highest and tends to 180°.[74]

Because the observed emission strongly depends on the temperature, it is important to locate the depth of the involved levels within the band gap of the oxyfluoride. In the following, DFT calculations by HF/LDA-GGA methods are used to estimate the density of states in the Ba_2InO_3F and $BaSrInO_3F$ compositions with either one oxygen vacancy ($Ba_8Sr_8In_8O_{23}F_8$) or two fluorine vacancies ($Ba_8Sr_8In_8O_{24}F_{62}$), in order to identify the electron density related to defects/anionic vacancies stabilizing the lone pair of In^+ ($5s^2$). The oxygen and fluorine vacancy formation energies were also calculated and discussed.

https://doi.org/10.1021/acs.inorgchem.5c04288
Inorg. Chem. 2026, 65, 3270−3285

3.4. DFT Calculations, Defect States in the Band Gap, and Mechanism of Photoluminescence

The E= f(k) dispersion curves (LDA-GGA methods) of Ba_2InO_3F and $BaSrInO_3F$ are represented in Figure S6, showing an indirect band gap between the M (valence band) and Γ (conduction band) points in the first Brillouin zone. The valence band shows a predominant O 2p character, while the In 5s orbitals present the largest contribution to the conduction band. One should mention that while the LDA-GGA functionals largely underestimate band gap values, a qualitative comparison between materials can still be made. A slight decrease in the band gap is underlined as Sr is partially substituted for Ba. Tauc plots obtained from diffuse reflectance spectra, reported in Figure S7, confirm this trend and yield experimental band gap values, which gradually decrease from 4.28 eV for Ba_2InO_3F to 4.08 eV for $BaSrInO_3F$.

Defect formation energies (oxygen or fluorine vacancy) were calculated for the Ba_2InO_3F and $BaSrInO_3F$ structures. Due to the difference in chemical potential between O and F, comparison of the formation energies of O and F vacancies for one given composition cannot be rigorously conducted. It is thus difficult to determine at this stage whether a given sample will preferentially form O or F vacancies. However, for a given defect (either O or F vacancy), it is possible to compare the evolution of both the formation energy and the defect levels' positions within the bandgap. This is represented in Figure S8. With partial Sr substitution, the fluorine vacancy defect is significantly more stabilized, while its formation energy remains relatively constant. On the contrary, the oxygen vacancy formation energy strongly increases for $BaSrInO_3F$ compared to the pure Ba compound, and the position of the oxygen vacancy defect within the bandgap is only very slightly lower in energy. The stabilization energy of an F vacancy seems independent of the composition, whereas the formation of an O vacancy appears less easy in $BaSrInO_3F$.

The evolution of partial densities of states of In and O orbitals for the structures containing a defect is represented in Figure 8, considering one oxygen vacancy (1 V_O) or two fluorine vacancies (2 V_F) in Ba_2InO_3F and $BaSrInO_3F$. Defect states (mainly p(O) and s(In) orbital mixing) related to oxygen and fluorine vacancies are systematically detected between the valence and the conduction bands. As previously described when discussing the formation energy of fluorine vacancies, defect states appear lower in energy in the Sr-containing phase. Moreover, as mentioned above, the energy positioning of the O vacancy defect states within the band gap does not evolve with Sr substitution. Besides, the DOS value for the defect states linked to oxygen vacancies is much higher in $BaSrInO_3F$. The unit cells in Figure 8 represent the structure alongside an isovalue of the electron density (in yellow) associated with the defect states only. It is located around indium and is characteristic of a $5s^2$ lone pair. Considering the oxygen vacancy hypothesis, a strong hybridization between In(sp) and the O(p) orbitals from the equatorial O atoms is clearly identified regardless of composition. This hybridization is significantly weaker in the F vacancy model, while the electron doublet ($5s^2$) is still active for both compositions.

On the basis of defect/anionic vacancy formation energies and DFT calculations, a photoluminescence mechanism based on defect centers in $Ba_{2-x}Sr_xInO_{3-y}F_{1-z}$ at RT and T = 10 K can be proposed. Because of the various anions' electronegativity, it is reasonable to consider that the stabilization of an oxygen defect would be deeper (near the valence band) than that of a fluorine defect (Figure 9a). It seems more difficult to create oxygen vacancies in $Ba_{2-x}Sr_xInO_3F$ than in Ba_2InO_3F, but the density of states of these oxygen defects in the band gap remains higher for $Ba_{2-x}Sr_xInO_{3-y}F_{1-z}$.

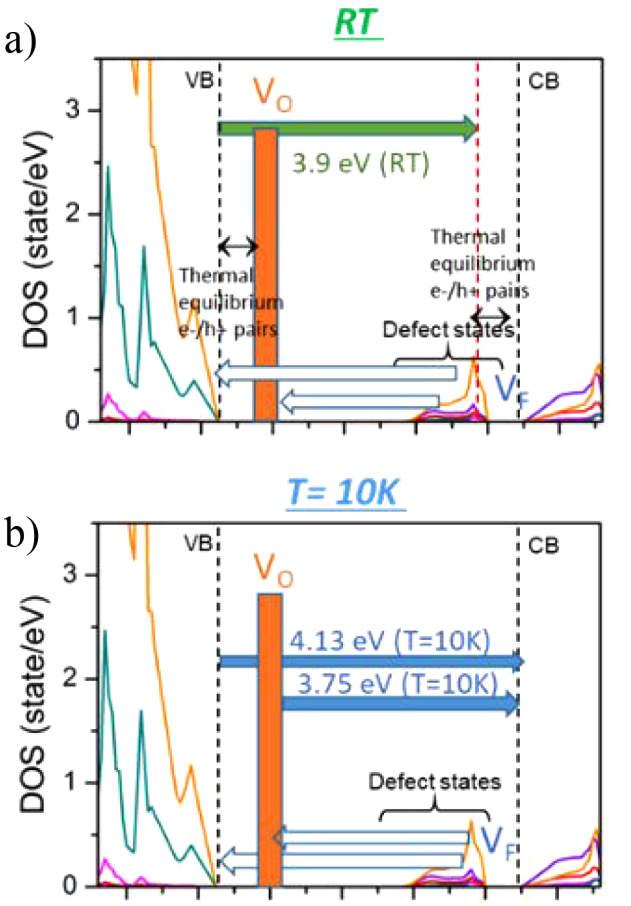

Figure 9. On the basis of DFT calculations, schematic representation a) at room temperature and b) at T = 10K of band diagrams for the $Ba_{1.2}Sr_{0.8}InO_{3-y}F_{1-z}$ composition with defect states related to the formation of oxygen and fluorine vacancies. The probable electronic transitions with excitation (full arrows) and emission (empty arrows) energies are mentioned.

As a localized level with high density of states, the oxygen vacancy defect level in $Ba_{2-x}Sr_xInO_{3-y}F_{1-z}$ could be regarded as a low-energy state near the valence band involved in the observed excitation at T = 10 K inducing photoluminescence. In this scenario at a low temperature, where the V_O defect is assumed to contribute to the luminescence profile of the compound, the excited electrons could reach the conduction band after stemming from the valence band ($\Delta E \approx 4.13$ eV) or from the oxygen vacancy defect level ($\Delta E \approx 3.75$ eV), leading to two bands on the excitation spectra (see Figures 9b and 7a,c).

Regarding the emission spectra at T = 10 K and a mechanism attributed to defect centers, the experimental band profile showcases one large and one asymmetric band centered at 450 (2.75 eV, T = 10 K) and at 480 (2.60 eV, T = 105 K) nm, respectively (blue-green curves in Figure 7b). Because of their asymmetric shapes, a second contribution at lower energy should occur and could involve the second defect associated with fluorine vacancy, with the defect energy state now below the conduction band. Both of these V_O/V_F defect

https://doi.org/10.1021/acs.inorgchem.5c04288
Inorg. Chem. 2026, 65, 3270−3285

states mixing monovalent indium (s,p) and oxygen p orbitals would be activated in the photoluminescence mechanism at T = 10 K.

Although the two sub-bands in both excitation and emission are distinguishable at very low temperatures, the excitation and emission spectra at room temperature (RT) display only single bands, albeit slightly asymmetric. Considering such a mechanism, at RT, a thermal equilibrium phenomenon, involving electron/hole pairs, should take place between the valence band and the O vacancy level, as well as between the conduction band and the F defect level. In this situation, only one excitation transition would be observed, from the valence band to the F defect state ($\Delta E \approx 3.9$ eV or 310 nm). The asymmetric shape of the excitation band on the high-energy side is probably due to the contribution of the valence band and the V_O defect. Concerning the large emission band, the defect states induced by the fluorine vacancy would be directly involved in the photoluminescence process. As Sr content increases, this V_F level is all the more stabilized and separated from the conduction band. On the In−O−In bond angle in the basal plane, the In(s,p)-O(p) hybridization increases and passes through a maximum for $Ba_{1.2}Sr_{0.8}InO_3F$ where fluorine vacancies can be stabilized, while the formation of an oxygen vacancy seems more difficult as the Sr content increases, considering the defect formation energies related to oxygen and fluorine vacancy. Consequently and on the basis of the electroneutrality of the composition, monovalent indium is also stabilized, part of the emission radiative process and systematically coupled with anionic vacancies, forming defect states which may be responsible for the global observed photoluminescence properties.

4. CONCLUSIONS

Singlecrystal and powder XRD analyses of the $Ba_{2-x}Sr_xInO_3F$ series reveal the occurrence of two In sites corresponding to distorted octahedra, which can be linked to square base pyramids. This results in anionic (O/F) disorder involving apical sites.

Annealing under air at high temperature shows a reduction in cell parameters, as well as a variation in the In distribution between two sites, which is connected to the anionic disorder and a decrease of the radiative properties. Taking such a change into account, the stabilization of monovalent indium, which helps pull the perovskite layers apart by Coulombic repulsion with the lone pair $5s^2$ associated with anionic vacancies in the apical site, has been considered.

The two In site occupancies and the O2−In−O2 bond angle evolve alongside the Sr content. The bond angle reflects the stabilization of the electron doublet, as well as the two alkaline earth sizes and bond valences. A maximum in the O2−In−O2 bond angle with a larger occupancy of the InB site is reached for the $Ba_{1.2}Sr_{0.8}InO_{3-y}F_{1-z}$ composition. This is associated with monovalent indium stabilization along with anionic vacancies and anionic disorder in the apical site. Furthermore, an almost similar alkaline-earth size and valence are observed between the two (Ba/Sr) sites in the vicinity of the (O/F) apical sites, leading one to also consider anionic disorder. Given the large difference in ionic radii, which induces geometric constraints, the mixed environment (Ba/Sr) is highly conducive to the destabilization of anionic sites as well as anionic disordering and creation of anionic vacancies linked to monovalent indium.

The F^- hopping phenomenon also becomes predominant in the case of $Ba_{1.2}Sr_{0.8}InO_{3-y}F_{1-z}$, where the increase in temperature largely brings out the ^{19}F NMR peak specific to the mixed (Ba/Sr) environment, containing a maximum of anionic vacancies at low temperature. This astonishing effect, showing the enhancement of resonance of the (Ba,Sr) mixed site with increasing temperature, is remarkably decreased in the case of $BaSrInO_{3-y}F_{1-z}$. An optimum is then still reached for the $Ba_{1.2}Sr_{0.8}InO_{3-y}F_{1-z}$ compound, evidencing a larger content of anionic vacancies at the (O/F) apical sites associated with an optimum of In^+ content.

Concerning the photoluminescence properties, a broad emission band ranging from 450 to 750 nm under ultraviolet excitation at 310 nm is observed. The corresponding intensity is visibly impacted by the Sr/Ba atomic ratio, but this ratio has no influence on the spectral distribution. A maximum intensity is still reached for $Ba_{1.2}Sr_{0.8}InO_{3-y}F_{1-z}$. The stabilization of monovalent indium coupled with the vacant anionic apical sites as defects seems to be the origin of the emission.

Finally, DFT calculations allowed for the identification of defect states arising from the hybridization between In(s,p) and O(p) orbitals, involving anionic (O/F) vacancies hosting the lone pair ($5s^2$) of monovalent indium. It seems more difficult to create an oxygen vacancy in the presence of Sr, but the energy positioning of the oxygen defects in the band gap does not depend on the composition. However, the F-vacancy defect energy level is stabilized more deeply in the band gap in the case of the Sr-rich oxyfluoride. The stabilization of defect states within the band gap should contribute to the broadband photoluminescence with a large Stokes shift, which is reflected in the 2D character of In-based oxyfluorides with a layered perovskite structure.

The stabilization of monovalent indium is concomitant with the generation of anionic vacancies (O/F), with fluorine vacancies being favored as Sr content increases up to an optimum rate. Mixed-anion compositions allow for the generation of anionic disorder and anionic mobility in 2D layer perovskites, which are often the seat of mixed ionic-electronic conductivity. The stabilization of In^+ in various Ruddlesden−Popper phases from 3D to 2D character must be investigated by following the self-trapped excitons and the fluorine/oxygen mobility, but also by considering the electronic conductivity, which could be enhanced by doping. Other elements, such as Sn^{2+}/Sn^{4+}, Sb^{3+}/Sb^{5+} with $5s^2$ electron doublet or Ti^{3+}/Ti^{4+} with d electrons stabilized in perovskite-related networks, constitute a relevant playground in the field of coupling ionic mobility and optical properties.

■ ASSOCIATED CONTENT

Supporting Information

The Supporting Information is available free of charge at https://pubs.acs.org/doi/10.1021/acs.inorgchem.5c04288.

Attribution of impurity peaks in $Ba_{1.4}Sr_{0.6}InO_{3-y}F_{1-z}$ (Figure S1); XRD-Rietveld refinement of the $Ba_{1.2}Sr_{0.8}InO_{3-y}F_{1-z}$ phase (Figure S2); unit cell a parameter and volume variation as a function of x-Sr content (Figure S3); ^{19}F MAS NMR and ^{19}F NMR spectra of $Ba_{1.2}Sr_{0.8}InO_3F$ (Figure S4); excitation spectra of the $Ba_{1.2}Sr_{0.8}InO_{3-y}F_{1-z}$ compound at T= 105 K and for various emission wavelengths (Figure S5); dispersion curves in the first Brillouin zone for the Ba_2InO_3F and $BaSrInO_3F$ compositions determined by LDA-GGA

https://doi.org/10.1021/acs.inorgchem.5c04288
Inorg. Chem. 2026, 65, 3270−3285

methods (Figure S6); Tauc plots representing [F(R) (Kubelka–Munk function = K(absorption)/S (Scattering) coefficients) x hν] $^{1/2}$ function for indirect band gap versus hν (Figure S7); evolution of formation energy of structural defects (Figure S8); room-temperature single-crystal XRD analysis of the $Ba_{1.22}Sr_{0.78}InO_{3-y}F_{1-z}$ compound with unit-cell parameters, atomic positions, occupancy, and isotropic/anisotropic parameters (Table S1); lattice parameters from powder X-ray diffraction for different values of Sr content (x) in $Ba_{2-x}Sr_xInO_{3-y}F_{1-z}$ (Table S2); a and c lattice parameters, interatomic distances, and O2–In–O2 bond angles for all studied compositions, extracted from single-crystal XRD measurements, with O1 and F sites reversed when InB site is considered (Table S3); room-temperature single-crystal XRD data analysis of $Ba_{2-x}Sr_xInO_{3-y}F_{1-z}$ compounds for varying values of Sr content (x) and two different annealing atmospheres, Ar and dry air (Table S4); and BVS calculations from $Ba_{2-x}Sr_xInO_{3-y}F_{1-z}$ single-crystal data analysis (Table S5) (PDF)

Accession Codes

Deposition Numbers 2502771–2502772, 2502775, and 2502777–2502778 contain the supplementary crystallographic data for this paper. These data can be obtained free of charge via the joint Cambridge Crystallographic Data Centre (CCDC) and Fachinformationszentrum Karlsruhe Access Structures service.

AUTHOR INFORMATION

Corresponding Author

Alain Demourgues – *Univ. Bordeaux, CNRS, Bordeaux INP, ICMCB, UMR5026, Pessac F-33608, France;* orcid.org/0000-0002-3828-8498; Email: alain.demourgues@icmcb.cnrs.fr

Authors

Alizée Deslandes – *Univ. Bordeaux, CNRS, Bordeaux INP, ICMCB, UMR5026, Pessac F-33608, France; Center for Optics, Photonics and Lasers (COPL), Université Laval, Québec, Quebec G1V 0A6, Canada;* orcid.org/0000-0001-5049-5361

Fouad Alassani – *Univ. Bordeaux, CNRS, Bordeaux INP, ICMCB, UMR5026, Pessac F-33608, France*

Stanislav Péchev – *Univ. Bordeaux, CNRS, Bordeaux INP, ICMCB, UMR5026, Pessac F-33608, France*

Véronique Jubera – *Univ. Bordeaux, CNRS, Bordeaux INP, ICMCB, UMR5026, Pessac F-33608, France;* orcid.org/0000-0002-2832-3958

Mathieu Duttine – *Univ. Bordeaux, CNRS, Bordeaux INP, ICMCB, UMR5026, Pessac F-33608, France;* orcid.org/0000-0002-6120-8716

Jacinthe Gamon – *Univ. Bordeaux, CNRS, Bordeaux INP, ICMCB, UMR5026, Pessac F-33608, France;* orcid.org/0000-0002-0888-4248

Antoine Villesuzanne – *Univ. Bordeaux, CNRS, Bordeaux INP, ICMCB, UMR5026, Pessac F-33608, France*

Leïlou Loiseau-Foucher – *Univ. Bordeaux, CNRS, Bordeaux INP, ICMCB, UMR5026, Pessac F-33608, France*

Etienne Durand – *Univ. Bordeaux, CNRS, Bordeaux INP, ICMCB, UMR5026, Pessac F-33608, France*

Alexandre Fargues – *Univ. Bordeaux, CNRS, Bordeaux INP, ICMCB, UMR5026, Pessac F-33608, France*

Complete contact information is available at: https://pubs.acs.org/10.1021/acs.inorgchem.5c04288

Funding

The authors thank the Région Aquitaine and Canada Excellence Research Chair in Photonic Innovation for PhD grant support, as well as additional contribution from the Mitacs Globalink program and the European Union's Horizon 2020 Research and Innovation Program under the Marie Skłodowska-Curie grant agreement no. 823941 (Funglass project).

Notes

The authors declare no competing financial interest.

ACKNOWLEDGMENTS

The authors wish to thank Stéphane Célerier and Laetitia Maziere (IC2MP, Poitiers, France) for conducting the ICP measurements. The authors also thank Helies Hyrondelle for F^- dosimetry data acquisition (ICMCB-CNRS, Talence, France). Finally, the authors acknowledge the CRISTAL beamline at Synchrotron Soleil for performing synchrotron data acquisition.

REFERENCES

(1) Ravi, V. K.; Mondal, B.; Nawale, V. V.; Nag, A. Don't Let the Lead Out: New Material Chemistry Approaches for Sustainable Lead Halide Perovskite Solar Cells. *ACS Omega* **2020**, *5* (46), 29631–29641.

(2) Arfin, H.; Kshirsagar, A. S.; Kaur, J.; Mondal, B.; Xia, Z.; Chakraborty, S.; Nag, A. Ns2 Electron (Bi3+ and Sb3+) Doping in Lead-Free Metal Halide Perovskite Derivatives. *Chem. Mater.* **2020**, *32* (24), 10255–10267.

(3) Zhao, X.-G.; Yang, J.-H.; Fu, Y.; Yang, D.; Xu, Q.; Yu, L.; Wei, S.-H.; Zhang, L. Design of Lead-Free Inorganic Halide Perovskites for Solar Cells via Cation-Transmutation. *J. Am. Chem. Soc.* **2017**, *139* (7), 2630–2638.

(4) Luo, J.; Li, S.; Wu, H.; Zhou, Y.; Li, Y.; Liu, J.; Li, J.; Li, K.; Yi, F.; Niu, G.; Tang, J. Cs2AgInCl6 Double Perovskite Single Crystals: Parity Forbidden Transitions and Their Application For Sensitive and Fast UV Photodetectors. *ACS Photonics* **2018**, *5* (2), 398–405.

(5) Tan, Z.; Li, J.; Zhang, C.; Li, Z.; Hu, Q.; Xiao, Z.; Kamiya, T.; Hosono, H.; Niu, G.; Lifshitz, E.; Cheng, Y.; Tang, J. Highly Efficient Blue-Emitting Bi-Doped Cs2SnCl6 Perovskite Variant: Photoluminescence Induced by Impurity Doping. *Adv. Funct. Mater.* **2018**, *28* (29), 1801131.

(6) Li, T.; Luo, S.; Wang, X.; Zhang, L. Alternative Lone-Pair Ns2-Cation-Based Semiconductors beyond Lead Halide Perovskites for Optoelectronic Applications. *Adv. Mater.* **2021**, *33* (32), 2008574.

(7) Li, Z.; Song, G.; Li, Y.; Wang, L.; Zhou, T.; Lin, Z.; Xie, R.-J. Realizing Tunable White Light Emission in Lead-Free Indium(III) Bromine Hybrid Single Crystals through Antimony(III) Cation Doping. *J. Phys. Chem. Lett.* **2020**, *11* (23), 10164–10172.

(8) Cheng, X.; Li, R.; Zheng, W.; Tu, D.; Shang, X.; Gong, Z.; Xu, J.; Han, S.; Chen, X. Tailoring the Broadband Emission in All-Inorganic Lead-Free 0D In-Based Halides through Sb3+ Doping. *Adv. Opt. Mater.* **2021**, *9* (12), 2100434.

(9) Xu, Z.; Jiang, X.; Cai, H.; Chen, K.; Yao, X.; Feng, Y. Toward a General Understanding of Exciton Self-Trapping in Metal Halide Perovskites. *J. Phys. Chem. Lett.* **2021**, *12* (43), 10472–10478.

(10) Jing, Y.; Liu, Y.; Zhao, J.; Xia, Z. Sb3+ Doping-Induced Triplet Self-Trapped Excitons Emission in Lead-Free Cs2SnCl6 Nanocrystals. *J. Phys. Chem. Lett.* **2019**, *10* (23), 7439–7444.

(11) Kshirsagar, A. S.; Arfin, H.; Banerjee, S.; Mondal, B.; Nag, A. Colloidal Sb3 ± Doped Cs2InCl5·H2O Perovskite Nanocrystals with Temperature-Dependent Luminescence. *J. Phys. Chem. C* **2021**, *125* (50), 27671–27677.

(12) Gong, Z.; Zheng, W.; Huang, P.; Cheng, X.; Zhang, W.; Zhang, M.; Han, S.; Chen, X. Highly Efficient Sb3+ Emitters in 0D Cesium Indium Chloride Nanocrystals with Switchable Photoluminescence through Water-Triggered Structural Transformation. *Nano Today* **2022**, *44*, 101460.
(13) Liu, X.; Zhang, W.; Xu, R.; Tu, J.; Fang, G.; Pan, Y. Bright Tunable Luminescence of Sb $^{3+}$ Doping in Zero-Dimensional Lead-Free Halide Cs $_3$ ZnCl $_5$ Perovskite Crystals. *Dalton Trans.* **2022**, *51* (26), 10029−10035.
(14) Oomen, E. W. J. L.; Smit, W. M. A.; Blasse, G. On the Luminescence of Sb $^{3+}$ in Cs $_2$ NaMCl $_6$ (with M = Sc,Y,La): A Model System for the Study of Trivalent s ^{2} Ions. *J. Phys. C: Solid State Phys.* **1986**, *19* (17), 3263−3272.
(15) Cao, L.; Jia, X.; Gan, W.; Ma, C.-G.; Zhang, J.; Lou, B.; Wang, J. Strong Self-Trapped Exciton Emission and Highly Efficient Near-Infrared Luminescence in Sb3 ± Yb3+ Co-Doped Cs2AgInCl6 Double Perovskite. *Adv. Funct. Mater.* **2023**, *33* (13), 2212135.
(16) Wu, H.; Lin, Z.; Song, J.; Zhang, Y.; Guo, Y.; Zhang, W.; Huang, R. Boosting the Self-Trapped Exciton Emission in Cs4SnBr6 Zero-Dimensional Perovskite via Rapid Heat Treatment. *Nanomaterials* **2023**, *13* (15), 2259.
(17) Lin, R.; Zhu, Q.; Guo, Q.; Zhu, Y.; Zheng, W.; Huang, F. Dual Self-Trapped Exciton Emission with Ultrahigh Photoluminescence Quantum Yield in CsCu2I3 and Cs3Cu2I5 Perovskite Single Crystals. *J. Phys. Chem. C* **2020**, *124* (37), 20469−20476.
(18) Smets, B. M. J.; Verlijsdonk, J. G.; Rutten, J. The Jahn-Teller Effect in the Excitation and Emission Spectra of Ba6Y2Al4O15: Sn2+ and Ba2YAlO5: Sn2+. *Mater. Res. Bull.* **1989**, *24* (4), 431−439.
(19) Kageyama, H.; Hayashi, K.; Maeda, K.; Attfield, J. P.; Hiroi, Z.; Rondinelli, J. M.; Poeppelmeier, K. R. Expanding Frontiers in Materials Chemistry and Physics with Multiple Anions. *Nat. Commun.* **2018**, *9* (1), 772−772.
(20) Sullivan, E.; Avdeev, M.; Vogt, T. Structural Distortions in Sr3-xAxMO4F (A = Ca, Ba; M = Al, Ga, In) Anti-Perovskites and Corresponding Changes in Photoluminescence. *J. Solid State Chem.* **2012**, *194*, 297−306.
(21) Needs, R. L.; Weller, M. T. Synthesis and Structure of Ba2InO3F: Oxide/Fluoride Ordering in a New K2NiF4 Superstructure. *J. Chem. Soc. Chem. Commun.* **1995**, 353−354.
(22) Needs, R. L.; Weller, M. T. Structure of Ba3In2O5F2 by Combined Powder X-Ray and Neutron Diffraction Analysis; Oxide/Fluoride Ordering in a Ruddlesden−Popper Phase. *J. Chem. Soc., Dalton Trans.* **1995**, No. 18, 3015−3017.
(23) Tarasova, N.; Animitsa, I. Protonic Transport in Oxyfluorides Ba2InO3F and Ba3In2O5F2 with Ruddlesden−Popper Structure. *Solid State Ionics* **2015**, *275*, 53−57.
(24) Needs, R. L.; Weller, M. T.; Scheler, U.; Harris, R. K. Synthesis and Structure of Ba2InO3X (X = F, Cl, Br) and Ba2ScO3F; Oxide/Halide Ordering in K2NiF4-Type Structures. *J. Mater. Chem.* **1996**, *6* (7), 1219−1224.
(25) Hector, A. L.; Hutchings, J. A.; Needs, R. L.; Thomas, M. F.; Weller, M. T. Structural and Mössbauer Study of Sr2FeO3X (X = F, Cl, Br) and the Magnetic Structure of Sr2FeO3F. *J. Mater. Chem.* **2001**, *11* (2), 527−532.
(26) Su, Y.; Tsujimoto, Y.; Matsushita, Y.; Yuan, Y.; He, J.; Yamaura, K. High-Pressure Synthesis, Crystal Structure, and Magnetic Properties of Sr2MnO3F: A New Member of Layered Perovskite Oxyfluorides. *Inorg. Chem.* **2016**, *55* (5), 2627−2633.
(27) Tsujimoto, Y.; Li, J. J.; Yamaura, K.; Matsushita, Y.; Katsuya, Y.; Tanaka, M.; Shirako, Y.; Akaogi, M.; Takayama-Muromachi, E. New Layered Cobalt Oxyfluoride, Sr2CoO3F. *Chem. Commun.* **2011**, *47* (11), 3263−3265.
(28) Tsujimoto, Y.; Yamaura, K.; Uchikoshi, T. Extended Ni(III) Oxyhalide Perovskite Derivatives: Sr2NiO3X (X = F, Cl). *Inorg. Chem.* **2013**, *52* (17), 10211−10216.
(29) Hyrondelle, H.; Terry, A.; Lhoste, J.; Tencé, S.; Lemoine, K.; Olchowka, J.; Dambournet, D.; Tassel, C.; Gamon, J.; Demourgues, A. Fluorine as a Key Element in Solid-State Chemistry of Mixed Anions 3d Transition Metal-Based Materials for Electronic Properties and Energy. *Chem. Rev.* **2025**, *125* (8), 4287−4358.
(30) Case, G. S.; Hector, A. L.; Levason, W.; Needs, R. L.; Thomas, M. F.; Weller, M. T. S. Powder Neutron Diffraction Structures and Mössbauer Studies of Some Complex Iron Oxyfluorides: Sr3Fe2O6F0.87, Sr2FeO3F and Ba2InFeO5F0.68. *J. Mater. Chem.* **1999**, *9* (11), 2821−2827.
(31) Gamon, J.; Bassat, J.-M.; Villesuzanne, A.; Duttine, M.; Batuk, M.; Vandemeulebroucke, D.; Hadermann, J.; Alassani, F.; Weill, F.; Durand, E.; Demourgues, A. Impact of Anionic Ordering on the Iron Site Distribution and Valence States in Oxyfluoride Sr2FeO3+xF1−x (x = 0.08, 0.2) with a Layered Perovskite Network. *Inorg. Chem.* **2023**, *62*, 10822.
(32) Tsujimoto, Y.; Matsushita, Y.; Hayashi, N.; Yamaura, K.; Uchikoshi, T. Anion Order-to-Disorder Transition in Layered Iron Oxyfluoride Sr2FeO3F Single Crystals. *Cryst. Growth Des.* **2014**, *14* (9), 4278−4284.
(33) van der Vorst, C. P. J. M.; Verschoor, G. C.; Maaskant, W. J. A. The Structures of Yellow and Red Indium Monochloride. *Acta Crystallogr. B* **1978**, *34* (11), 3333−3335.
(34) Staffel, T.; Meyer, G. The Mono-, Sesqui-, and Dibromides of Indium: InBr, In2Br3, and InBr2. *Z. Für Anorg. Allg. Chem.* **1987**, *552* (9), 113−122.
(35) Jones, R. E.; Templeton, D. H. The Crystal Structure of Indium (I) Iodide. *Acta Crystallogr.* **1955**, *8* (12), 847−847.
(36) Tarasova, N. A.; Animitsa, I. E. S. Hydration, and Electrical Properties of Oxyfluoride Ba2InO3F. *Russ. J. Electrochem.* **2015**, *51* (5), 401−405.
(37) Petříček, V.; Dušek, M.; Palatinus, L. Crystallographic Computing System JANA2006: General features. *Z. Für Krist. - Cryst. Mater.* **2014**, *229* (5), 345−352.
(38) Bruker *APEX4, SAINT and SADABS*; Bruker AXS Inc.: Madison, Wisconsin, USA, 2021.
(39) Dolomanov, O. V.; Bourhis, L. J.; Gildea, R. J.; Howard, J. A. K.; Puschmann, H. OLEX2: A Complete Structure Solution, Refinement and Analysis Program. *J. Appl. Crystallogr.* **2009**, *42* (2), 339−341.
(40) Sheldrick, G. M. SHELXT − Integrated Space-Group and Crystal-Structure Determination. *Acta Crystallogr. Sect. Found. Adv.* **2015**, *71* (1), 3−8.
(41) Sheldrick, G. M. Crystal Structure Refinement with SHELXL. *Acta Crystallogr., Sect. C:Cryst. Struct. Commun.* **2015**, *71* (1), 3−8.
(42) Thurber, K. R.; Tycko, R. Measurement of Sample Temperatures under Magic-Angle Spinning from the Chemical Shift and Spin-Lattice Relaxation Rate of 79Br in KBr Powder. *J. Magn. Reson.* **2009**, *196* (1), 84−87.
(43) Massiot, D.; Fayon, F.; Capron, M.; King, I.; Le Calvé, S.; Alonso, B.; Durand, J.-O.; Bujoli, B.; Gan, Z.; Hoatson, G. Modelling One- and Two-Dimensional Solid-State NMR Spectra. *Magn. Reson. Chem.* **2002**, *40* (1), 70−76.
(44) Makuła, P.; Pacia, M.; Macyk, W. How To Correctly Determine the Band Gap Energy of Modified Semiconductor Photocatalysts Based on UV−Vis Spectra. *J. Phys. Chem. Lett.* **2018**, *9* (23), 6814−6817.
(45) Heyd, J.; Scuseria, G. E. Efficient Hybrid Density Functional Calculations in Solids: Assessment of the Heyd−Scuseria−Ernzerhof Screened Coulomb Hybrid Functional. *J. Chem. Phys.* **2004**, *121* (3), 1187−1192.
(46) Krukau, A. V.; Vydrov, O. A.; Izmaylov, A. F.; Scuseria, G. E. Influence of the Exchange Screening Parameter on the Performance of Screened Hybrid Functionals. *J. Chem. Phys.* **2006**, *125* (22), 224106.
(47) Perdew, J. P.; Burke, K.; Ernzerhof, M. Generalized Gradient Approximation Made Simple. *Phys. Rev. Lett.* **1996**, *77* (18), 3865−3868.
(48) Stoliaroff, A.; Jobic, S.; Latouche, C. PyDEF 2.0: An Easy to Use Post-Treatment Software for Publishable Charts Featuring a Graphical User Interface. *J. Comput. Chem.* **2018**, *39* (26), 2251−2261.

https://doi.org/10.1021/acs.inorgchem.5c04288
Inorg. Chem. 2026, 65, 3270−3285

(49) Shannon, R. D. Revised Effective Ionic Radii and Systematic Studies of Interatomic Distances in Halides and Chalcogenides. *Acta Crystallogr. A* **1976**, *32* (5), 751−767.
(50) Dutton, S. E.; Hirai, D.; Cava, R. J. Low Temperature Synthesis of *Ln*OF Rare-Earth Oxyfluorides through Reaction of the Oxides with PTFE. *Mater. Res. Bull.* **2012**, *47* (3), 714−718.
(51) Glätzle, M.; Schauperl, M.; Hejny, C.; Tribus, M.; Liedl, K. R.; Huppertz, H. Orthorhombic HP-REOF(RE = Pr, Nd, Sm − Gd) − High-Pressure Syntheses and Single-Crystal Structures (RE = Nd, Sm, Eu). *Z. Für Anorg. Allg. Chem.* **2016**, *642* (20), 1134−1142.
(52) Tsujimoto, Y.; Nakano, S.; Ishimatsu, N.; Mizumaki, M.; Kawamura, N.; Kawakami, T.; Matsushita, Y.; Yamaura, K. Pressure-Driven Spin Crossover Involving Polyhedral Transformation in Layered Perovskite Cobalt Oxyfluoride. *Sci. Rep.* **2016**, *6* (1), 36253.
(53) Gutau, W.; Müller-Buschbaum, H. Über ein neues Halogen-ooxoindat: Ba3In2O5Cl2 mit Sr3Ti2O7-Struktur. *Z. Für Anorg. Allg. Chem.* **1990**, *584* (1), 125−128.
(54) Sadoc, A.; Body, M.; Legein, C.; Biswal, M.; Fayon, F.; Rocquefelte, X.; Boucher, F. NMR Parameters in Alkali, Alkaline Earth and Rare Earth Fluorides from First Principle Calculations. *Phys. Chem. Chem. Phys.* **2011**, *13* (41), 18539−18550.
(55) Fukushima, E. *Experimental Pulse NMR: A Nuts and Bolts Approach*; CRC Press: Boca Raton, 2018.
(56) Wang, F.; Grey, C. P. Probing the Mechanism of Fluoride-Ion Conduction in LaF3 and Strontium-Doped LaF3 with High-Resolution 19F MAS NMR. *Chem. Mater.* **1997**, *9* (5), 1068−1070.
(57) Murakami, M.; Mineshige, A. 19F NMR Studies on Ionic Conduction Pathways in Tysonite-CeF3. *J. Phys. Chem. Solids* **2022**, *161*, 110432.
(58) Martineau, C.; Fayon, F.; Legein, C.; Buzaré, J.-Y.; Corbel, G. Solid-State ^{19}F MAS NMR Investigation of Fluoride Ion Mobility in Lead Fluorides: Correlation with Anionic Conductivity. *Chem. Mater.* **2010**, *22* (4), 1585−1594.
(59) Chaminade, J. P.; Garcia, A.; Gaewdang, T.; Pouchard, M.; Grannec, J.; Jacquier, B. Reversible Photoionization Process in Luminescent Ce3+ Doped Elpasolite-Type Fluoroindates. *Radiat. Eff. Defects Solids* **1995**, *135* (1−4), 137−141.
(60) Cornu, L.; Gaudon, M.; Veber, P.; Villesuzanne, A.; Pechev, S.; Garcia, A.; Jubera, V. Discussion on the Structure Stability and the Luminescence Switch under Irradiation of a Ce-Doped Elpasolite Compound. *Chem.−Eur. J.* **2015**, *21* (13), 5242−5251.
(61) Gaudon, M.; Andron, I.; Demourgues, A.; Rodriguez, V.; Fargues, A.; Durand, E.; Chiron, A.; Frayret, C.; Jubera, V. Emission Colours of Bistable Photochromic Compounds: Ce-Doped Alkaline (Rb, K, Na)-Indium Fluorides. *Mater. Adv.* **2022**, *3* (18), 7061−7071.
(62) Blasse, G.; Grabmaier, B. C. *Luminescent Materials*; Springer: Berlin Heidelberg: Berlin, Heidelberg, 1994. DOI: .
(63) Andriessen, J.; Marsman, M.; Van Eijk, C. W. E. Ab Initio Study of the Stokes Shift of the Ns-Np Transition of Tl+ and In+ in KCl, Jahn-Teller Effect in the Nsnp Configuration. *J. Phys.: Condens. Matter* **2001**, *13* (24), 5597.
(64) Jiang, F.; Wu, Z.; Lu, M.; Gao, Y.; Li, X.; Bai, X.; Ji, Y.; Zhang, Y. Broadband Emission Origin in Metal Halide Perovskites: Are Self-Trapped Excitons or Ions? *Adv. Mater.* **2023**, *35* (51), 2211088.
(65) Li, S.; Luo, J.; Liu, J.; Tang, J. Self-Trapped Excitons in All-Inorganic Halide Perovskites: Fundamentals, Status, and Potential Applications. *J. Phys. Chem. Lett.* **2019**, *10* (8), 1999−2007.
(66) Luo, J.; Wang, X.; Li, S.; Liu, J.; Guo, Y.; Niu, G.; Yao, L.; Fu, Y.; Gao, L.; Dong, Q.; Zhao, C.; Leng, M.; Ma, F.; Liang, W.; Wang, L.; Jin, S.; Han, J.; Zhang, L.; Etheridge, J.; Wang, J.; Yan, Y.; Sargent, E. H.; Tang, J. Efficient and Stable Emission of Warm-White Light from Lead-Free Halide Double Perovskites. *Nature* **2018**, *563* (7732), 541−545.
(67) Green, R. L.; Avdeev, M.; Pierre, V. Structural Distortions and Self-Activated Photoluminescence in Reductively Annealed Ba2Sr-GaO4F. *J. Solid State Chem.* **2019**, *276*, 376−381.
(68) Ranfagni, A.; Mugnai, D.; Bacci, M.; Viliani, G.; Fontana, M. P. The Optical Properties of Thallium-like Impurities in Alkali-Halide Crystals. *Adv. Phys.* **1983**, *32* (6), 823−905.
(69) Oomen, E. W. J. L.; Smit, W. M. A.; Blasse, G. Jahn-Teller Effect in the Sb3+ Emission in Zircon-Structured Phosphates. *Chem. Phys. Lett.* **1984**, *112* (6), 547−550.
(70) Arfin, H.; Nag, A. Origin of Luminescence in Sb3± and Bi3 ± Doped Cs2SnCl6 Perovskites: Excited State Relaxation and Spin−Orbit Coupling. *J. Phys. Chem. Lett.* **2021**, *12* (41), 10002−10008.
(71) Folkerts, H. F.; Blasse, G. Luminescence of Pb2+ in SrTiO3. *Chem. Mater.* **1994**, *6* (7), 969−972.
(72) Drickamer, H. G.; Klick, D. I. High Pressure Studies of Luminescent Phenomena. *J. Less-Common Met.* **1978**, *62* (C), 381−396.
(73) Fukuda, A. Jahn-Teller Effect on the Structure of the Emission Produced by Excitation in the A Band of KI: Tl-Type Phosphors. Two Kinds of Minima on the Γ 4 − (T 1 u 3) Adiabatic Potential-Energy Surface. *Phys. Rev. B* **1970**, *1* (10), 4161−4178.
(74) Srivastava, A. M.; Ackerman, J. F.; Beers, W. W. On the Luminescence of Ba5*M*4O15(*M*=Ta5+, Nb5+). *J. Solid State Chem.* **1997**, *134* (1), 187−191.

https://doi.org/10.1021/acs.inorgchem.5c04288
Inorg. Chem. 2026, 65, 3270−3285